Quantifying eddy diffusivity in the Labrador Sea in a mixing-length theoretical framework

Joseph William Ribeiro

24736848

Supervisor:

Eleanor Frajka-Williams

May 2015

MSci Oceanography

SOES6071: MSci Advanced Independent Research Project

Word count: 9992

National Oceanography Centre
NATURAL ENVIRONMENT RESEARCH COUNCIL

UNIVERSITY OF Southampton

Abstract

Mesoscale eddies are effective large-scale stirrers which provide a crucial connection between mean flow scales, such as those in the Labrador Sea (LS) boundary currents, and small scale dissipative processes. The relationship between currents and mesoscale eddies is not straightforward, however, as currents have the potential to both produce and disintegrate eddies. This study uses altimetric and AR7W hydrographic data to estimate mixing lengths and relative lateral eddy diffusivities in the LS in order to determine whether there is suppression of mixing by the LS boundary currents. In the West Greenland Current (WGC) across AR7W, a poor relationship is identified between an altimeter-derived inverse suppression factor and both mixing length ($R = 0.4769$, $p = 0.0335$) and relative lateral eddy diffusivity ($R = 0.2293$, $p = 0.3309$). This is interpreted as evidence for unsuppressed mixing. A close relationship is found between surface Eddy Kinetic Energy and both mixing length ($R= 0.9598$, $p < 0.0001$) and relative lateral eddy diffusivity ($R =0.9918$, $p < 0.0001$) in the WGC. Due to the weak tracer gradient across isopycnals stemming laterally from the Labrador Current, results are robust only in one cross section which crosses the WGC. Nonetheless, this study makes a first quantification of mixing length and eddy diffusivity across a LS boundary current.

Acknowledgments

I would like to thank both Eleanor Frajka-Williams and Alberto Naveira Garabato for always being very willing to provide advice and for guiding me through this project. Data used in this project was provided by AVISO, NOAA NODC Ocean Climate Laboratory and Fisheries and Oceans Canada. Data analysis was carried out in Mathworks MATLAB®.

Contents

1: Motivation

The LS is one of the few regions in the world where deep convection occurs. Deep convection in the LS is the process where surface water sinks to depths of 1000m or greater to form the water mass known as Labrador Sea Water (LSW; Lilly et al., 1999). The most important consequence of LSW formation is that it forms the sinking limb of the Atlantic Meridional Overturning Circulation (AMOC), and therefore imposes controls on the rate and character of the Atlantic overturning (Hoffmann & Rahmstorf, 2009). Concerns exist that if deep convection is inhibited by sufficient freshwater (FW) forcing, the AMOC could collapse and may restabilise under a different equilibrium state where no deep convection occurs in the LS and the warm North Atlantic Drift is diverted away from Western Europe. The climate in the North Atlantic is approximately 4 degrees warmer than equivalent latitudes in the Pacific Ocean due to the warmth provided by the North Atlantic Drift (Rahmstorf, 1996). This means without deep convection in the LS, Western Europe could effectively enter a mini ice-age.

As well as potentially driving the AMOC, the formation of LSW also influences mid-depth mixing and circulation in subpolar basins (Yashayev et al., 2007). Finally, transport between the subpolar and subtropical gyres is modulated by the formation of LSW (Curry & McCartney, 2001). Therefore there is potential for ocean and climate feedbacks on various timescales in response to changes in LSW formation.

The extent of LSW formation over any one winter depends on the buoyancy input to the LS and the relative amount of atmospheric and oceanic forcing acting against this (Mizoguchi et al., 2003). We predict large changes in the FW export from the Arctic due to continued global warming, and some of this FW will exit the Arctic via the LS (McGeehan & Maslowski, 2011). Although the supply of FW from the Arctic is expected to increase, the relative threat this poses to deep convection will depend on how strongly this water is mixed out of the LS boundary currents. For this reason we attempt to quantify the mixing across the WGC and LC in this study.

2: The Labrador Sea

2.1: Circulation in the Labrador Sea

The LS has a cyclonic circulation, and is encircled by two main boundary currents. Parallel to the West coast of Greenland is the West Greenland Current (WGC), which flows around Cape Desolation from the Irminger Sea and carries fresh, cold water ($\theta \approx 1.8°C$, $S \leq 34.5$) from the Nordic seas. Below this cold water is a current of warmer and saltier Irminger Sea Water (ISW: $\theta \approx 4.5°C$, $S \approx 34.95$). Parallel to the coast of Labrador is the Labrador Current (LC) which flows South-East out of the LS along the coast of Canada. The LC is often referred to as three separate currents: the coastal LC, the shelf break LC and the deep LC. The shelf break LC is fresh and cold ($\theta \approx 1.5°C$, $S \leq 34$), whilst the deep LC has a signature of modified ISW, and the coastal LC is composed mainly of buoyant outflow from Hudson strait (Straneo & Saucier, 2008; Cuny et al., 2002). Crucially, the shelf-break WGC and LC are more buoyant than the water in the central LS, lending them the potential to regulate deep convection.

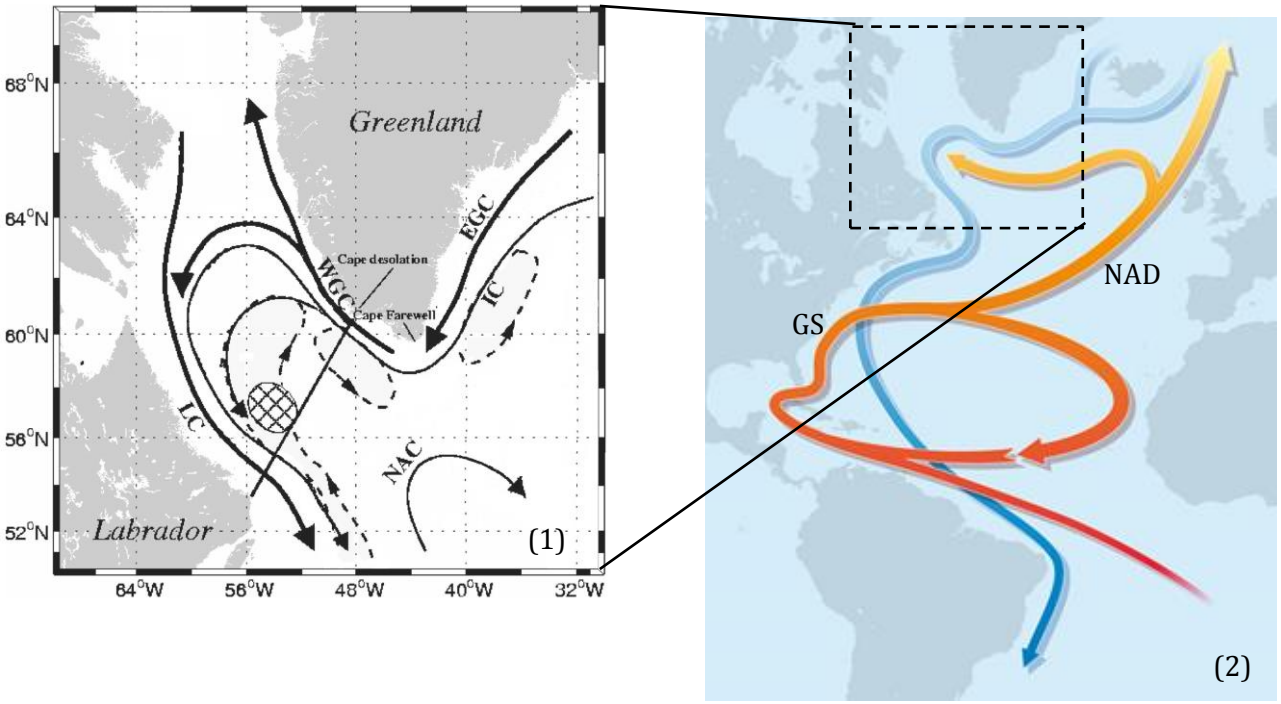

Figure 1: Circulation in Labrador Sea. WGC and LC are introduced in main body, whilst EGC, IC and NAC are East Greenland Current, Irminger Current and North Atlantic Current respectively. The region of deep convection is approximately depicted by shaded ellipse although the bounds of this region will vary year on year. Straight black line is AR7W transect. Modified from Chanut et al., 2008. Figure 2: The AMOC. Red arrows show surface currents including the Gulf stream (GS) and North Atlantic Drift (NAD), which terminate with deep convection in the arctic and LS. Blue arrows show return flow at depth. Modified from Marotzke (2012).

2.2: Controls on deep convection

Deep convection requires both atmospheric and oceanic preconditioning. On the gyre scale, isopycnals in the region of deep convection will dome towards the surface, causing a sharper surface density gradient from November onwards (see figures 2 and 3; Mizoguchi et al., 2003). By bringing the thermocline closer to the surface it can be broken down more effectively, however deep convection also requires significant cooling by dry, cold continental winds that prevail from Canada (Schmidt & Send, 2007) predominantly during periods of higher North Atlantic Oscillation (NAO) index (Curry & McCartney, 2001).

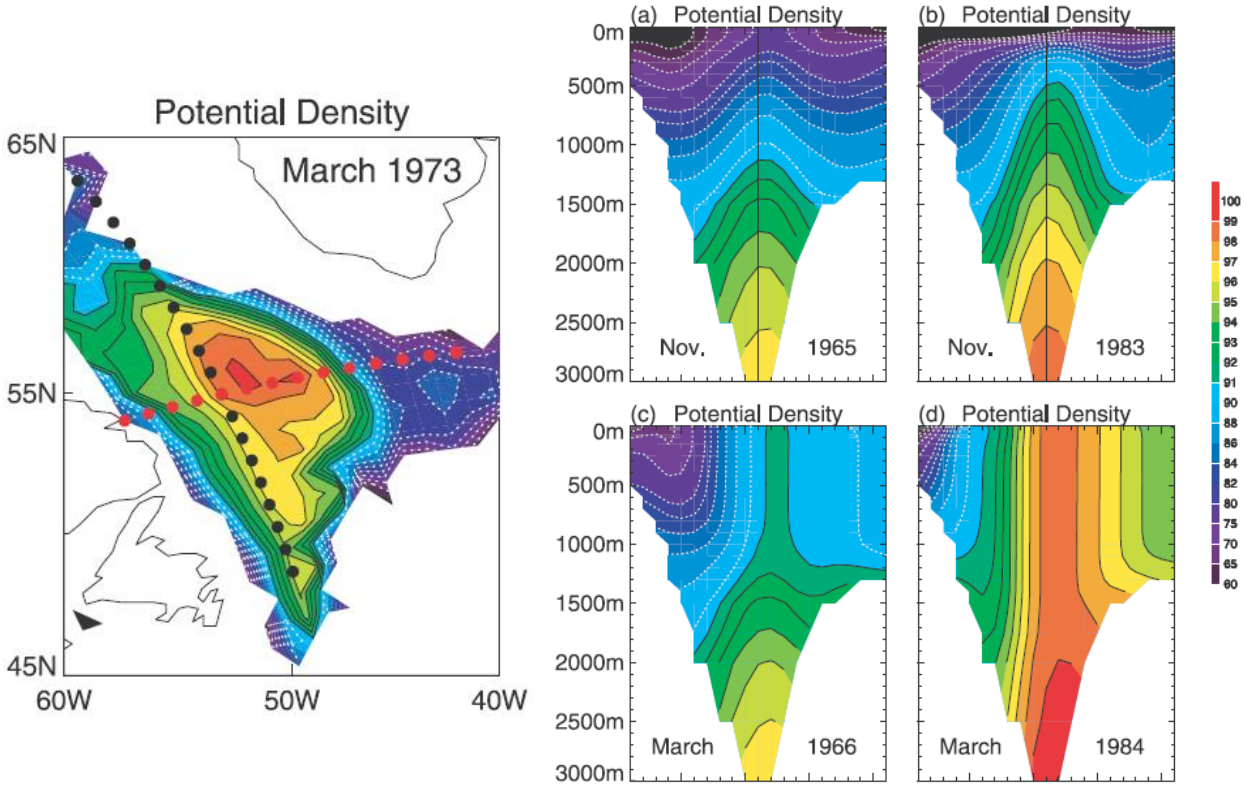

Figures 3 and 4a-d: Surface potential density (ρ_θ – 27 (kg/m^3) x 100) and potential density observed during preconditioning (4a-c) and active deep convection (4d). X-axis on 4a-d is distance along black line of points in figure 3. From Mizoguchi et al., 2003.

Oceanic preconditioning also occurs on the smaller eddy and plume scales (Mizoguchi et al., 2003). Mesoscale eddies are effective large-scale stirrers which provide a crucial connection between mean flow scales in the boundary currents and small scale dissipative processes (Tang et al., 1996). Studies have attributed the inhibition of deep convection over the central-to-

northern LS to eddies produced by the WGC, and to a lesser extent the LC (Kawasaki & Hasumi, 2014). Although both the LC and WGC predominantly flow along isobaths, eddies do often form in the currents and can mix into the central LS (Kawasaki & Hasumi, 2014). Subsequently they transport buoyancy out of the boundary currents and into the central LS, constraining deep convection to an area (see figure 1) of reduced eddy kinetic activity (Katsman et al., 2004; The Lab Sea Group, 1998).

LS eddies are separated into three categories: Firstly, Convective Eddies (CEs), which are generated seasonally by baroclinic instability of the rim current around the convection area (Eden & Böning, 2002). CEs are small (O ~10km) with a lifetime of less than one month (Kawasaki & Hasumi, 2014). Secondly, Boundary Current Eddies (BCEs) are generated by boundary current baroclinic instability and are of a similar size and duration, but occur throughout the year (Kawasaki & Hasumi, 2014). Finally warm, saline Irminger Rings (IRs) are formed perennially in the WGC, however it is not clear whether they are formed by barotropic or baroclinic instability, or a mixture (Gelderloos et al., 2011; Kawasaki & Hasumi, 2014). IRs are longer lived features which are closer to 40-50km in diameter and dominate the north-eastern LS, preventing deep convection from occurring there (Kawasaki & Hasumi, 2014).

2.3: Sources of FW to the Labrador Sea

We are concerned with the flux of buoyancy into the LS as either heat or FW, but since the LS boundary currents originate from the Arctic, we expect buoyancy changes to be dominated by reduced salinity. As an approximate estimate based on several models, a FW forcing of the order of 0.1 Sv may be adequate to collapse the AMOC (Hoffmann & Rahmstorf, 2009). This value varies depending on the relative emphasis placed on the different processes driving the AMOC (e.g. wind-driven upwelling) and the subsequent AMOC stability in the model chosen (Hoffmann & Rahmstorf, 2009). There are five primary changing sources of FW to the Arctic and Subarctic basins: Arctic Sea Ice, Greenland Ice Sheets, Bering Strait inflow, river runoff and changes in the water cycle.

The Greenland Ice Sheet neighbours the LS, but is expected to be relatively stable in the near-term. Still, an estimate based on several models predicts Greenland melt flux to increase from 0.018 to 0.033 Sv over the period 1970–2080, a significant export compared to sea-ice melt (Dickson et al., 2007; Lindsay & Zhang 2005).

The conclusion of various coupled climate modelling studies is that Arctic Ocean sea-ice will decrease in volume over the 21st century regardless of our change in greenhouse gas emissions (Dickson et al., 2007; Lindsay & Zhang 2005). The expected loss of 8500 km^3 of Arctic sea ice in 100 years associated with a 1% increase in CO_2 partial pressures per year is equivalent to a continued average FW input to the ocean of 0.0027 Sverdrups (Sv) over this period, i.e. a continuation of the trends we have observed since 1950 (Dickson et al., 2007). By 2100 we also expect a 37% increase in FW import into the Arctic from the Pacific via the Bering Strait by 2100, equivalent to a 0.03Sv increase in freshwater flux (Haak et al., 2005).

Model predictions quantify between 0.01-0.02 Sv increase in river discharge into the Arctic by 2050 (Wu et al., 2005). These predictions have not yet been observed,

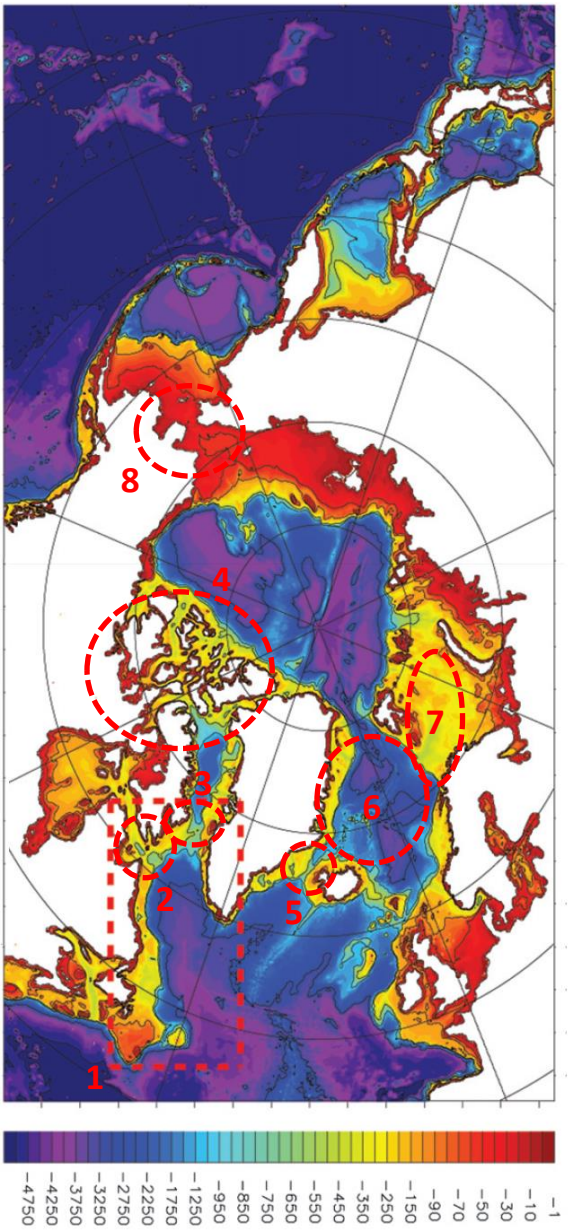

Figure 5: Bathymetric map centred on the Arctic. Locations of importance are labelled as follows: 1: Labrador Sea, 2: Hudson Strait, 3: Davis Strait, 4: CAA, 5: Fram Strait, 6: Greenland Sea, 7: Barents Sea, 8: Bering Strait. Modified from McGeehan & Maslowski, 2011.

however it is believed that observed changes have been predominantly driven by an increase in the intensity of the NAO and AO (Arctic Oscillation) (Dickson et al., 2000). An intensification of the global hydrological cycle may also indirectly cause a freshening of the LS, however analyses yield variable and sometimes contradictory results. Still, the majority of evidence does indicate an intensifying water cycle (Huntington, 2006).

There are therefore several potential sources with a large combined uncertainty in the predicted amount of FW entering to the LS, as well as significant uncertainty in the FW forcing required to collapse the AMOC.

2.4: Pathways of FW to the Labrador Sea

Buoyancy from the Arctic mainly enters the LS via the WGC and LC, although the path from the Arctic occurs via several basins. FW enters the WGC primarily through the Barents Sea and Fram Strait (Dickson et al., 2007). The Hudson Outflow contributes approximately 15% to the flow of the LC, and 50% of the FW content, and most of this outflow originates from the Canadian Arctic Archipelago (CAA) and Davis Strait (Straneo & Saucier, 2008).

The exchanges we see between the Arctic basins are by no means fixed. By 2100 the southward outflow through the CAA is expected to increase by almost 50% as the sea-ice transport reduces.

Fram strait ice outflows are significant contributors to the freshening of WGC (Kwok et al., 2004). We expect no change in Fram Strait-Barents Sea export as increase in liquid FW export is balanced by reduced sea ice export through the region (Dickson et al., 2007).

The LC and WGC

ISW is modified by its passage from the WGC to the LC, as the WGC bifurcates into two weaker currents around the north-western LS before joining the LC. To the North, this weak circulation may be slow enough for surface cooling to allow this water to mix along isopycnals with fresh Baffin Island Water originating from the Arctic, whilst the deeper Southern

bifurcation may supply a small amount of buoyancy to the LS as it mixes with the interior LS (Cuny et al., 2002).

Schmidt & Send (2006) found that seasonal pulses of FW in the LS could only be attributed to have come from an approximately coincidental seasonal FW pulse in the WGC (Schmidt & Send, 2007). Precipitation-evaporation, net local sea ice melt and vertical FW mixing terms were too small to explain the observed seasonal variability in the LS salinity. The timing of the main FW pulse coincided with a pulse in the WGC, whereas the seasonality in the LC could not explain the seasonal freshening observed in the LS. It is therefore suspected that 60% of the seasonal FW comes from the WGC boundary current (Schmidt & Send, 2007).

Myers (2005) also found that only 6-8% of the FW exported from the Canadian Arctic actually enters the LS, further suggesting the dominant supplier of FW to the LS is the WGC (Myers, 2005). The model used by Myers (2005) was eddy permitting, however it was relatively coarse (1/3°) and may not have adequately resolved the small scale phenomena (CEs and BCEs) we now recognise as important today. A higher resolution model was used to repeat the study, which found that the dominant exchange was onshore flow of water from the LS interior into the LC (McGeehan & Maslowski, 2011). The study did, however, identify periodic eddy events which exported a jet of FW into the region of deep convection. These events inhibited deep convection when occurring at the right time and location. A weak correlation ($R^2 = 0.25$) was also identified between the FW export through Davis Strait and deep convection in the LS, consistent with the previous belief that much of the FW exported to the LC does in fact stay on the shelf (McGeehan & Maslowski, 2011). Consequently, we currently expect that the WGC is the dominant pathway for buoyancy to enter the LS, supplied with FW from the Arctic (via the Irminger Sea) and Greenland.

As a first hypothesis, we therefore propose that ***the amount of mixing as quantified by the eddy diffusivity is greater across the WGC than the LC.***

Thomsen et al. (2013) apply linear stability analysis to model observations of the LC, however this method cannot be used quantify the mixing across the boundary current unless it is a purely linear flow. Since eddies are relatively common in the ACC, and parts of the boundary currents are known to form eddies, there is a need to quantify boundary current mixing from real observations instead of simply assuming non-linear dynamics are insignificant.

The rate of dispersion of floats, such as the PALACE floats analysed by Cuny et al. (2002), can be related to an eddy diffusivity parameterisation. Whilst useful, these Lagrangian diffusivities are of limited use when parameterising Eulerian eddy diffusivity in large scale ocean models (Ferrari & Nikurshin, 2010). In this study, we use altimetric and hydrographic data in a mixing-length based analysis to quantify a relative eddy diffusivity kc_e^{-1} in the LS.

3: Theory

3.1: Diffusivity

Turbulence is often described as enhanced diffusion (Ferrari and Nikurashin, 2010), as it moves tracer parcels erratically, allowing for more effective molecular diffusion. The complex turbulent process is often represented by the eddy diffusivity k. In this study, we parameterise the turbulent flux of potential vorticity (PV) down a PV gradient with a flux-gradient relation. The relationship between an across-jet tracer gradient $(\partial\bar{\varphi})/\partial Y$ and tracer perturbations from the mean φ' is used:

Equation (1) $$\overline{v'\varphi'} = -k\frac{\partial\bar{\varphi}}{\partial Y}$$

where overbars represent averaging in time and in the along-jet dimension, and v' is the across-jet velocity perturbation (with a mean of 0 by definition).

Holloway (1986), Keffer and Holloway (1988) and Stammer (1998) first estimated sea surface eddy diffusivity from satellite altimetry as the product of an eddy mixing length (L_{mix}) and an eddy velocity scale (U_{eddy}). L_{mix} was assumed to be proportional to the size of eddies, and this length was combined with U_{eddy} calculated from SSH gradients by geostrophic

approximation. The studies found that k peaked where eddy velocity was largest: in the core of strong currents.

More recently, Marshall et al (2006) estimated the surface k field in the Antarctic Circumpolar Current (ACC) through numerical modelling. Their approach involved using altimeter SSH derived velocities to model the advection of a tracer, with results identifying the highest k in the equatorward flank of the ACC jets as opposed to in the cores of the ACC jets. This has been interpreted by some as being enhanced surface mixing occurring in an outcropping critical layer where phase speed of Rossby waves approximately matches the mean zonal flow speed (Naveira Garabato et al., 2011).

Unlike molecular diffusivity, eddy diffusivity may be influenced by large scale currents, yet this effect is commonly overlooked in the literature (Naveira Garabato et al., 2011). In their analysis Ferrari and Nikurashin (2010) acknowledge that eddies tend to propagate upstream at a speed proportional to that of the mean flow. Because eddies follow potential vorticity gradients, eddies tend to propagate upstream of the mean current. The effect of this upstream propagation is to advect much of the tracer into the mean flow of the current before much cross-stream mixing is able to occur, and this is currently believed to be the reason for apparently enhanced k in the flanks of the ACC jets relative to the core of the jets. Ferrari and Nikurashin (2010) expect that their results apply equally well to tracer transport across any permanent current system, such as that of the LS boundary currents.

The main result of Ferrari and Nikurashin (2010) is that k can be derived from altimeter SSH (h) observations as:

Equation (2)
$$k = 0.32 \frac{g}{|f|} \frac{\overline{(h'^2)}^{0.5}}{1+8|\nabla\bar{h}|^2/\overline{|\nabla h'|^2}}$$

where h' is the eddy departure of h from its long-term mean $\bar{h}$, f is the Coriolis parameter and g is acceleration due to gravity. The result means that eddy mixing across a mean current is not simply proportional to eddy fluctuations in SSH alone, rather the mixing depends on the ratio of

mean kinetic energy to eddy kinetic energy (EKE). The denominator acts to suppress the mixing such that when $8\left|\nabla\bar{h}\right|^2/\overline{|\nabla h'|^2}$ is O(1), mixing suppression becomes significant. Chelton et al (2007) also find this ratio to characterise the degree of non-linearity of eddies in a region, meaning suppression is expected if eddies are non-linear. Naveira Garabato et al (2011) use a similar but inverse term of $(1 + 4U_m^2EKE^{-1})^{-1}$, determined from ADT-derived surface velocities, where U_m is the mean velocity. The term $(1 + 4U_m^2EKE^{-1})^{-1}$ is referred to hereafter as the inverse suppression factor (ISF), and is smaller in currents with greater suppression of EKE. EKE is calculated as half the u and v covariance $0.5\langle u^2 + v^2\rangle$. The analytical model upon which equation (2) is based assumes that there is no shear in the mean flow, and for that reason should only be applied to large ocean currents where the scale separation between the mean flow and the eddy scale is large enough for the mean flow shear to be ignored. In the LS it is unlikely that the separation between the eddy scale and mean flow scale is distinct enough to justify calculating k in the LS from altimeter SSH in equation 2. Still, the distinct scale separation between the background tracer gradient and tracer gradients associated with eddies allows us to use the same approach as Naveira Garabato et al. (2011).

3.2: Mixing length theory

In this study we employ the method used by Naveira Garabato et al (2011), which is based on mixing length theory. Naveira Garabato et al (2011) confirmed firstly that k is suppressed within thermohaline fronts of the Antarctic Circumpolar Current (ACC) due to a reduced mixing length resulting from eddy propagation relative to the mean flow, and secondly confirmed that L_{mix} is not simply proportional to the physical scale of eddies. Whilst suppression of eddy mixing was the dominant regime, the study identified unique sites termed 'leaky jet segments' where suppression was absent due to the interaction of the ACC mean flow with topographic features. The mean flow surrounding leaky jet segments was found to have non-parallel structure (meanders) on length scales comparable to eddy length scales, and these leaky jet segments contributed disproportionally to the eddy induced overturning of the ACC. We apply the same

method to the LS to investigate whether LS jets form a barrier to eddy mixing or whether jets in the LS are 'leaky'.

Mixing length theory was first introduced by Prandtl (1925) in which temperature T was decomposed as:

Equation (3) $$T = \overline{T} + T'$$

where $\overline{T}$ is the slowly varying component and T' is the fluctuating component (perturbation from the mean). If a parcel of water with temperature $\overline{T}$ is stirred vertically a distance ξ' along a temperature gradient $\partial T/\partial z$ before mixing and losing its original characteristics, the equivalent temperature fluctuation is:

Equation (4) $$T' = -\xi' \frac{\partial \overline{\mathrm{T}}}{\partial z}$$

Armi and Stommel (1983) hypothesised that horizontal (lateral) mixing due to mesoscale eddying should cause Fickian diffusion of a smooth tracer gradient with random-walk-like tracer dispersal. In this case, there should be a Gaussian distribution of tracer about the smoothed tracer gradient (which we find to approximately be the case – see section 5.5.3) with a standard deviation that quantifies the turbulent mixing length L_{mix} when normalised to the tracer gradient $|\nabla_n \theta_m|$.

This method of estimating L_{mix} has been frequently adopted, most recently by Polzin (2005) and Naveira Garabato et al (2011) whereby:

equation (5) $$L_{mix} = \frac{\theta_{RMS}}{|\nabla_n \theta_m|}$$

where θ_{RMS} is the standard deviation of a tracer (i.e. Conservative Temperature) fluctuation along a potential density (ρ_θ) surface produced by eddy stirring of the background gradient of the tracer θ_m, and ∇_n is the gradient operator on the same ρ_θ surface.

Equation (5) is based in a triple Reynolds decomposition by Joyce (1978), which provides an approach for investigating the role of diffusive processes in the mean, mesoscale, and microscale groups of turbulence. The following diagram from Garrett (2001) explains the role of mesoscale activity in the spectrum of length scales in the ocean:

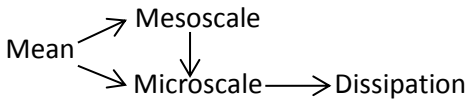

Although these arrows are not necessarily one-way, the dominant path to dissipation is via the mesoscale; the flux associated with vertical modes and internal waves is several orders of magnitude smaller than that produced by balanced eddies. Observational (Ledwell et al., 1993) and numerical (Gent & McWilliams 1990) studies also show that eddies transport temperature laterally with little diapycnal mixing. Ferrari & Polzin (2005) argue that for this reason, tracer variance in *equation (5)* is likely to be the product of lateral mixing by mesoscale eddies. Further details justifying the validity of *equation (5)* to estimate eddy mixing can be found in appendix B of Naveira Garabato et al. (2011).

Armi and Stommel (1983) propose that the magnitude of k is proportional to this mixing length L_{mix} and a velocity fluctuation scale U_e of the turbulence. This same relationship is most recently defined in Naveira Garabato et al (2011) as:

Equation (6) $$k = c_e U_e L_{mix}$$

where c_e is a mixing efficiency constant, the value of which depends on how effectively eddy stirring translates to mixing, as well as depending on the method used to derive L_{mix} .

As a second hypothesis, we contend that ***eddy diffusivity is unsuppressed in the core of the WGC, whilst suppression of eddy diffusivity by the mean flow occurs in the core of the LC.***

4: Data

This project uses four datasets. Primarily used is the Atlantic Repeat Hydrography Line 7. The repeat transect, known as AR7W, consists of 308 CTD profiles at regular stations taken annually between 2002-2008 from Newfoundland (53°40' N, 55°30'W), to the west coast of Greenland (60°30'N, 48°15'W), provided by Fisheries and Oceans Canada. These profiles are analysed alongside selected transects from 4901 seaglider profiles in the LS, taken between 2003-2005 and available from the NOAA NODC Ocean Climate Laboratory.

Also used are all-satellite optimal interpolation daily maps of Absolute Dynamic Topography (ADT), and *u* and *v* geostrophic velocities provided by AVISO on a 1/4° x 1/4° grid.

Before making any calculations, glider data has been finely interpolated onto 0.25 dbar pressure intervals, whilst AR7W data is provided on regular 1 dbar intervals.

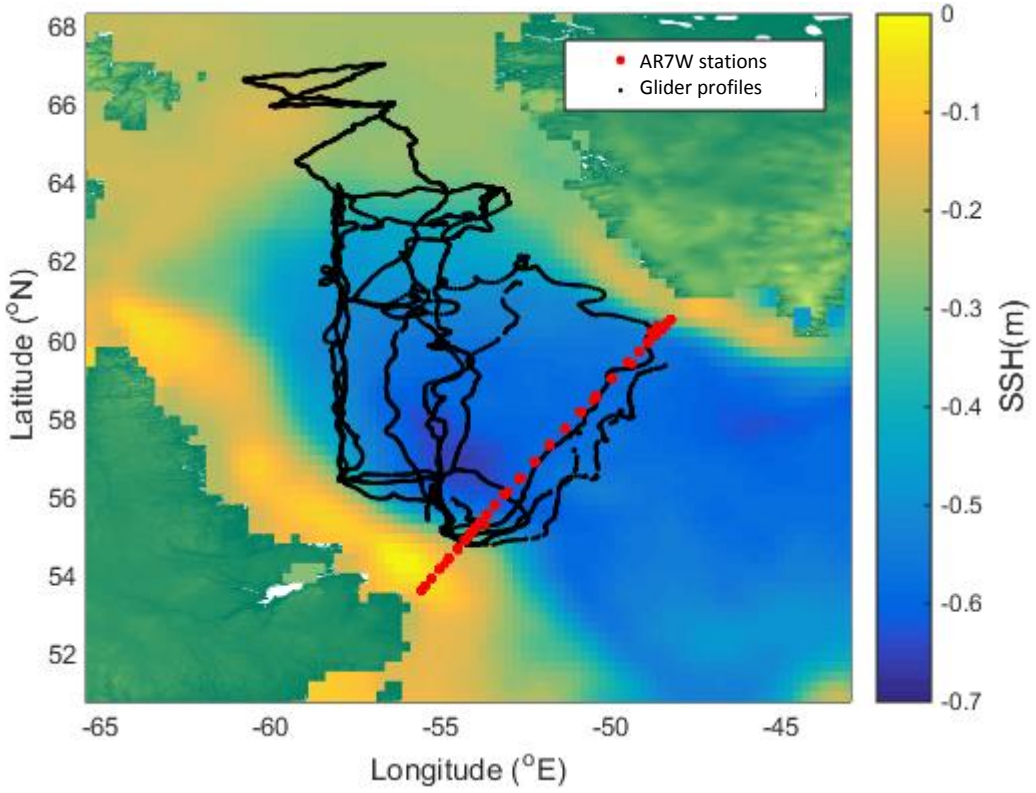

Figure 6: Mean ADT (h) with overlaid AR7W stations (red) and glider profiles (black).

T-S diagram of the Labrador Sea

AR7W data has been divided evenly at 52°W into North and South halves, hereafter referred to as AR7W-North and AR7W-South. Figures 7a-b are T-S diagrams of all data across AR7W-North and AR7W-South. Since the AR7W transect is sampled at quasi-regularly distanced stations focused mostly on the shelf break front, these stations arguably show evidence of gaps in T-S space in the surface kilometer, indicating that limited mixing is occurring between water masses on the shelf and off the shelf. These gaps in T-S space are slightly clearer across AR7W-South, suggesting that suppression of mixing may be occurring in the LC.

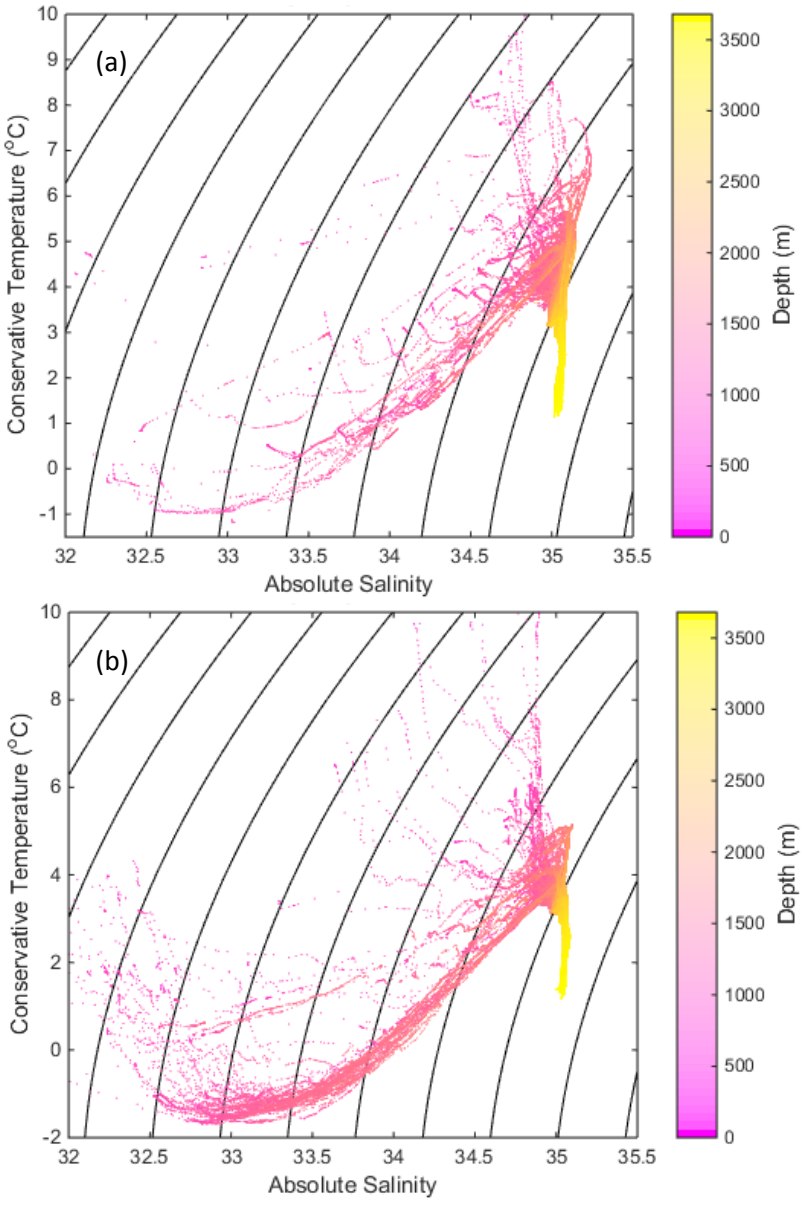

Figures 7a-b: T-S diagram of (a) AR7W-North and (b) AR7W-South.

5: Methods

The interaction between eddies and the LS boundary currents has not been a major focus in the literature, which instead centres on the different sources of EKE to the central LS and to the control this EKE has on deep convection. The mixing-length based method employed in this study has been applied to the LSW core in the Eastern North Atlantic by Cunningham & Haine (1995), however no such observational estimates exist within in the LS. We provide a first estimate of the depth varying k in the LS using equation (1). Ideally, *equation (5)* and thus equation (1) should be applied across a neutral density surface, however we apply the calculations across a ρ_θ surface as both surfaces are approximately equivalent within a confined basin of similar hydrography. We opt for Conservative Temperature (CT) as our tracer of choice, however resulting L_{mix} are nearly identical when using Absolute Salinity (AS) as a tracer.

5.1: Definition of across-jet distance *Y* using SSH and DH

In order to calculate the gradient $\partial T/\partial Y$ of a tracer along any across-jet transect, the across-jet distance Y of each CTD or glider profile must first be determined. If possible, this across-jet distance would be determined from DH (specifically, DH integrated from 200dbar to 50dbar $\mathrm{DH}\int_{200}^{50}$ for reasons given later on in section 5.1), however a reliable monotonic relationship between across-jet distance and DH (between any limits of integration) only occurs across the shelf-break jet. Neither SSH or DH vary monotonically from the coast to the centre of the LS, although the across-jet SSH gradient was found to be a more robust indicator of the across-jet distance than DH. The relationship between DH and bathymetric depth was found to be very variable depending on the section of LS front being crossed, mainly because of strong latitudinal variation in DH. This meant that reordering profiles in DH space frequently rearranged the profiles incorrectly. Due to the non-monotonic cross-frontal variability of both DH and SSH, we define the across-jet distance differently to Naveira Garabato et al (2011).

With 1D linear interpolation, the original maps of ADT were firstly interpolated onto the times of each data profile. The position of the boundary current jet was then identified to be the maximum ADT gradient (by combining the magnitude of $\partial h/dx$ and $\partial h/dy$). The coordinates for

the SSH-derived jet position were then finely interpolated, and the across-jet distance was taken to be the distance from each station to the nearest section of jet. In order to avoid mistakenly identifying eddy-induced SSH gradients as the jet SSH gradient, a 'valid jet region' was characterised as anywhere within 30km of any 750m-2000m isobath, as this depth range encompasses the shelf break in the majority of cases. An exception exists in the Northern LS, where the WGC bifurcates to form two weak currents connecting the WGC to the LC. The northernmost bifurcation lies between the 1000m and 2000m isobaths, whilst the southern bifurcation runs along the 3000m isobath approximately (Cuny et al., 2002). In all glider and AR7W transects included in this report, the across-jet distance *Y* has an origin relative to the shelf break jet.

In a linear 3D model analysis, Tang et al. (1996) found boundary currents on the shelf to be predominantly baroclinic, whilst towards the open sea the boundary currents are predominantly barotropic. This justifies using the SSH-based method above to define the across-jet distance as the larger shelf break jets, which are the focus in this report, have a strong SSH signature. This finding may also serve to explain why neither ADT or DH are completely monotonic from the coast to the central LS.

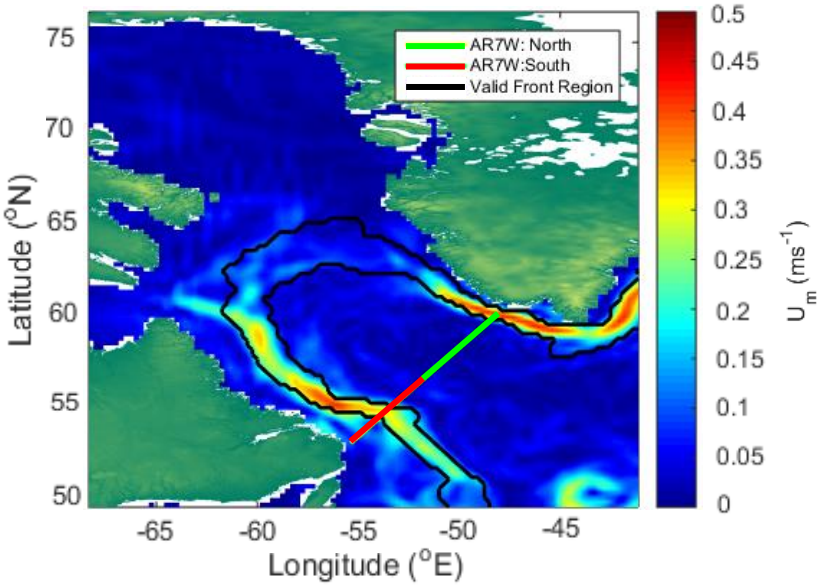

Figure 8: Mean Velocity in the Labrador Sea from ADT. Red and Green lines are AR7W-South and AR7W-North respectively, whilst thick black line indicates region in which the shelf-break jet was identified from the ADT gradient.

The above method allows profiles to be spaced appropriately in terms of the across-jet distance, however since the resulting transects still contained eddies, a process was applied to all data transects (both AR7W and glider) to remove these eddies. Firstly, the relationship between SSH and DH along each transect was fitted with a cubic spline, where a DH coordinate of specific volume anomaly (δ) integrated from 200 dbar to 50 dbar was chosen. Justifications for this coordinate are provided below. At each profile along the transect, the SSH standard deviation from the seasonal mean SSH was calculated over the 21 year time series, assumed to be an "eddy standard deviation". For each profile, SSH was predicted from DH using the SSH-DH spline fit (see figure 10a). An eddy was identified as any predicted SSH more than one "eddy standard deviation" away from the mean seasonal SSH at the location of the glider, and data from this profile would be discarded (see figure 10b). This avoided introducing tracer variability from the unmixed cores of eddies in the L_{mix} calculation (*equation 5*). The threshold of 1 standard deviation in SSH is an arbitrary choice, however it is a relatively conservative threshold which usually disposes of the entire eddy even when applied to weak eddies.

Included in figures 10-11 is an example of the procedure applied to glider transect 12, illustrating the effective removal of an eddy along this transect. The accuracy of this procedure depended on the spline fit between SSH and DH, which was robust for all data used, but was more effective for shorter glider transects with little latitudinal variability.

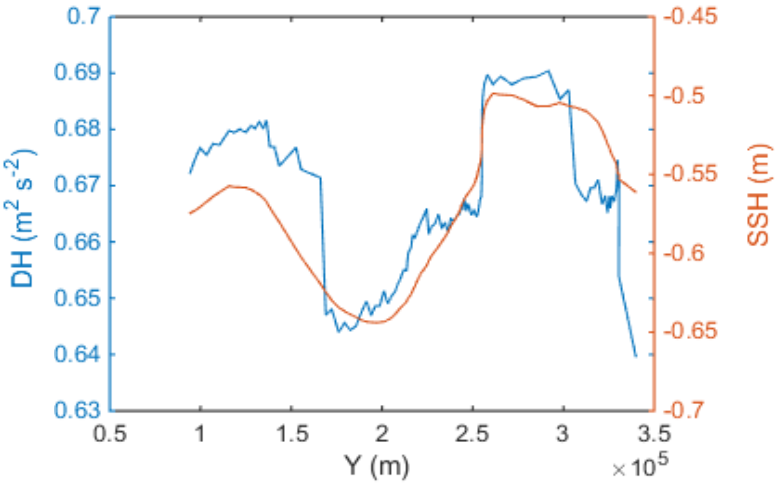

Figure 9: Interpolated SSH and DH (integrated from 200 dbar to 50 dbar) along glider transect 14d. Note how SSH provides a smoothed estimate of DH. Because of the lower resolution in SSH, it is more accurate to estimate SSH from in-situ DH measurements.

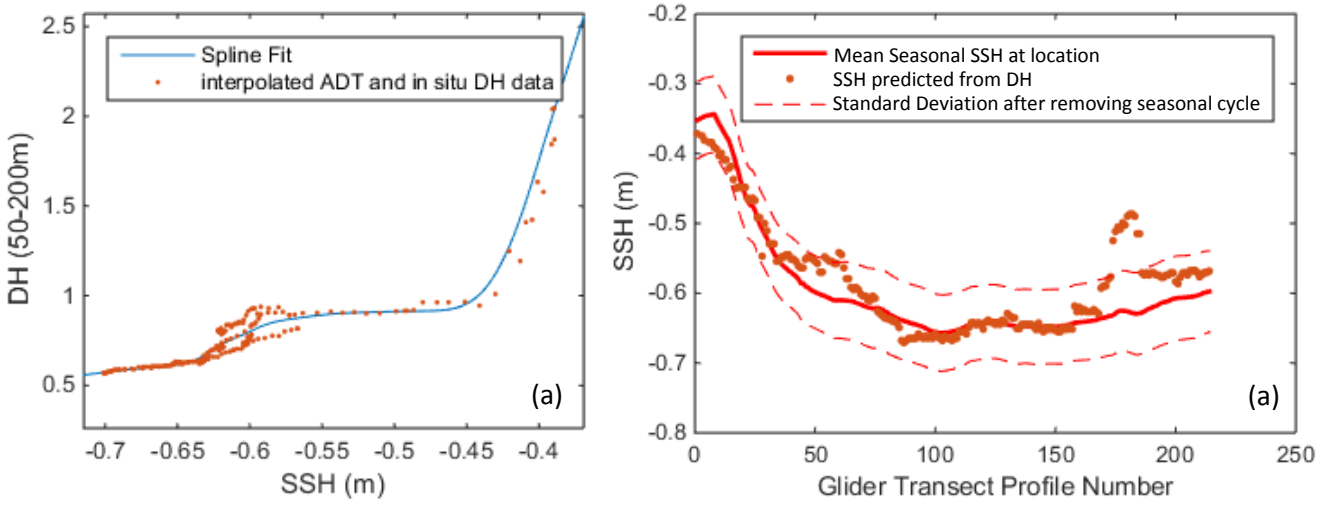

Figure 10a-b: (a) Spline fit between SSH and DH for glider transect 12. (b) Mean SSH at time of year along glider transect 12 (solid red line) and one standard deviation associated in seasonally detrended SSH at location (dashed red line). Orange points are SSH predictions based on in situ DH measurement.

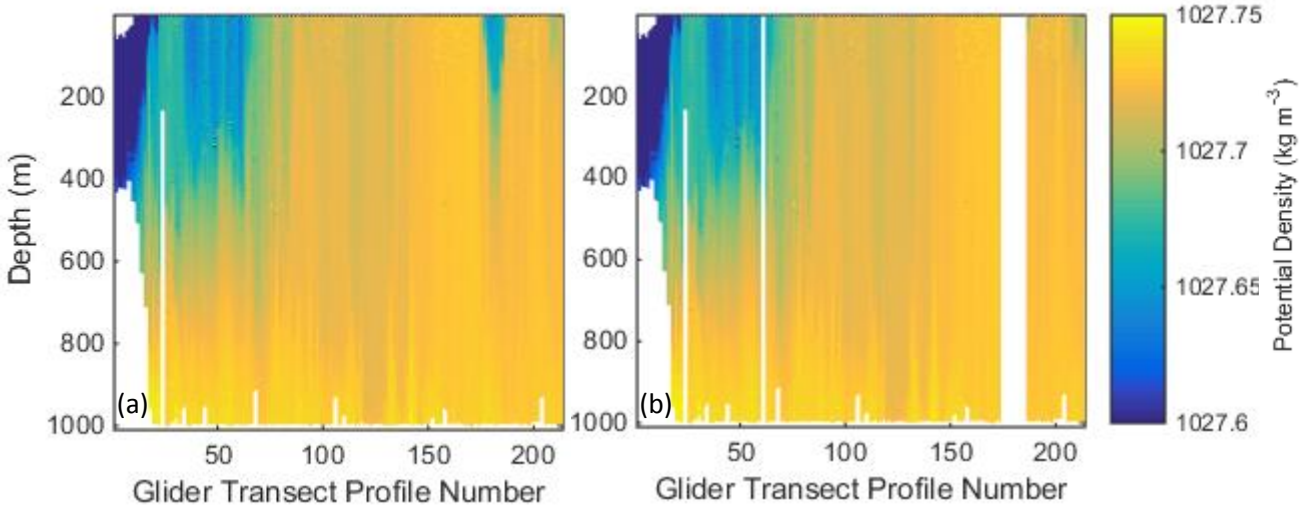

Figure 11a-b: Potential density along glider transect 12 (a) before and (b) after removing eddies.

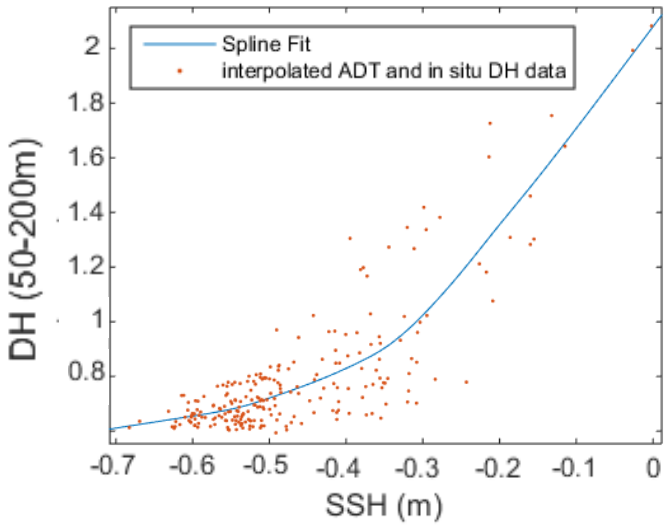

Figure 12: Plot of the DH-SSH relationship used to remove eddies from the AR7W dataset.

DH coordinates of specific volume anomaly (δ) integrated from 200 dbar to 50 dbar, defined as $\phi_{200}^{50} = \int_{200}^{50} \delta dp$, were chosen to estimate SSH from DH.

Because the above procedure attempts to obtain a SSH estimate from DH, we identified the range of limits that yield the strongest correlation between SSH and DH. Ideally, the range of pressures chosen should avoid the influence of atmospheric forcing at the surface, meaning it would be sensible to exclude pressures above 50 dbar in the DH calculation. It can be seen from the plots below that a strong linear relationship between SSH and DH exists between 200 dbar to 50 dbar, without compromising the number of gliders to which this pressure range is applicable (including the shallow glider profiles on the continental shelf).

All correlations below 10m have a p value of less than 0.01. With respect to degrees of freedom, the scale of ocean variability will limit the number of independent realisations made by our glider profiles used in the correlations below. This variability will occur over the eddy scale (approximately 50km for IRs, the largest category of LS eddies), whilst glider profiles are spaced at approximately 3km intervals. Since A minimum of 3489 glider profiles are used in the regressions plotted in figure 13, the number of independent realisations will be at an approximate minimum of 3489 x (3/50) = 209. This is equivalent to 209 -2 -1 = 206 degrees of freedom, which qualifies all correlations as significant at the 0.1% significance level (Williams, 1959).

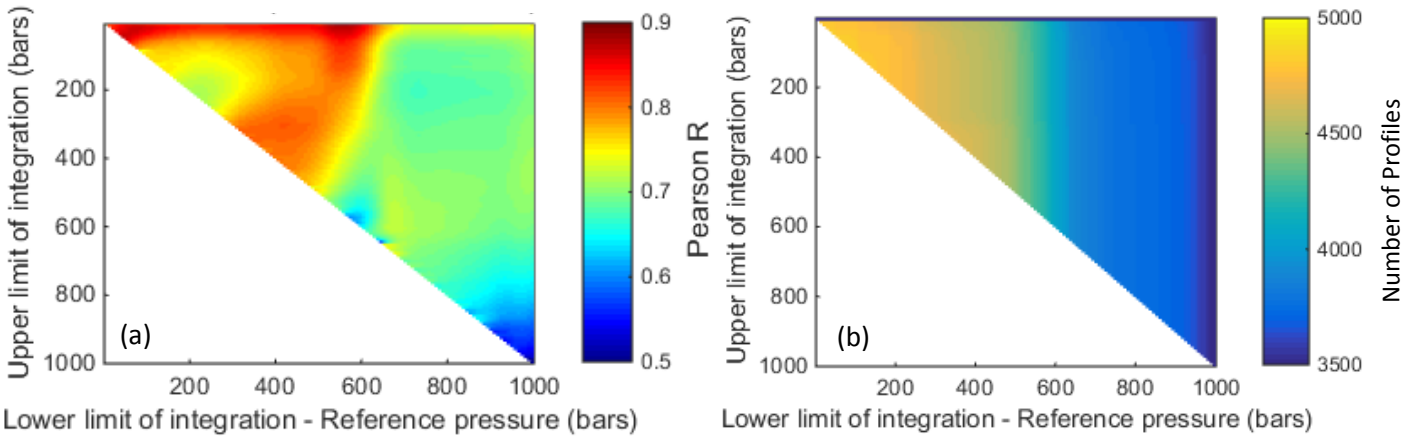

Figures 13a-b: (a) Correlation coefficient between SSH and DH between all possible limits of integration from the surface to 1000 dbar and (b) Number of glider profiles within limits of integration.

5.2: L_{mix}

After rearranging by Y, transects are interpolated from pressure coordinates onto ρ_θ coordinates. After mapping onto a ρ_θ-Y grid, the gradient $d\theta/dY$ is estimated using a cubic spline fit, whilst θ_{RMS} from this spline fit is calculated as one standard deviation of θ within a window ΔY on each ρ_θ surface. Justifications for the choice of ΔY and spline smoothness are given in section 5.5. Finally, L_{mix} is calculated as per *equation (5)*.

5.3: U_{eddy}

The eddy velocity scale U_{eddy} is defined as one standard deviation in time of the across-jet velocity, and is also derived using the method of Naveira Garabato et al (2011). For each glider and AR7W station, the across-jet bearing is identified as perpendicular to the mean velocity vector over the 21 year ADT-derived surface velocity time series. From this time series, the across-jet components of the daily surface velocity vectors were firstly extracted. Because transects predominantly cut across the jet, these surface across-jet velocities could not be projected to depth using DH-derived thermal wind, meaning several intermediate steps were taken. The second step involved making spline fits of the SSH-DH relationship for each pressure along each transect, as well as spline fits of the SSH-ρ_θ relationship. Since DH is integrated downwards, the strength of this SSH-DH relationship increases with pressure (see figure 14). Thirdly in order to obtain the geostrophic shear across the jet, the 21-year ADT time series was interpolated onto two locations 500m upstream and 500m downstream of the mean velocity vector at each station. Fourth, using the relationship between SSH and DH at each depth, the pressure-varying DH was calculated at each station, allowing the geostrophic velocity to be calculated relative to the surface for each station, time and depth. Fifth, these geostrophic velocities are added to the cross frontal component of surface velocities in order to estimate the velocity standard deviation at each station and depth. Finally, the relationship between SSH and potential density was used to calculate the time series of depth-varying potential density in order to map the velocity standard deviations calculated in step 5 onto the potential density grid used in the L_{mix} calculation.

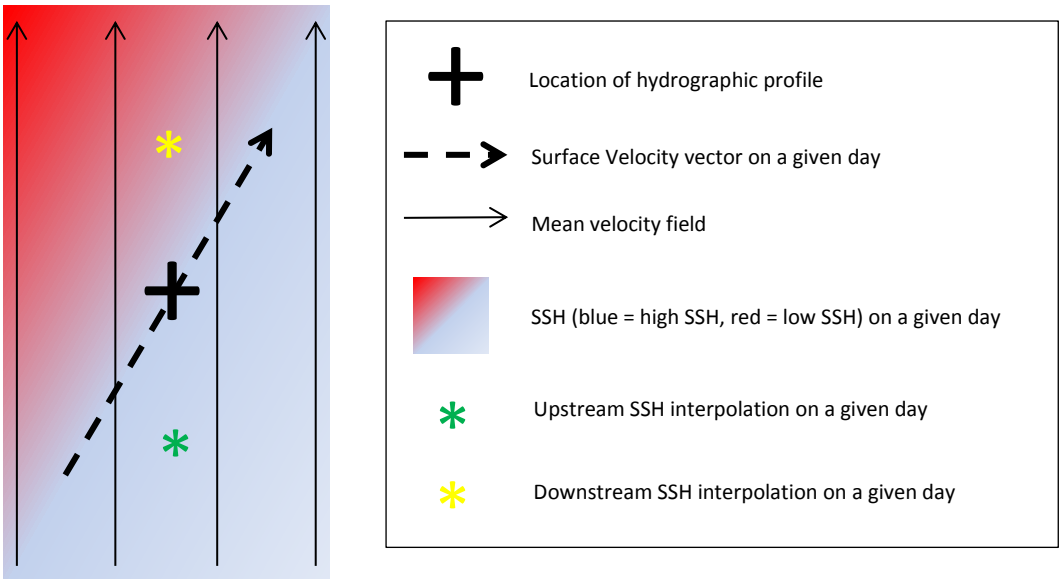

Figure 14a: Schematic illustrating the application of step 3 in the calculation of U_{eddy} to an instantaneous SSH field on a given day.

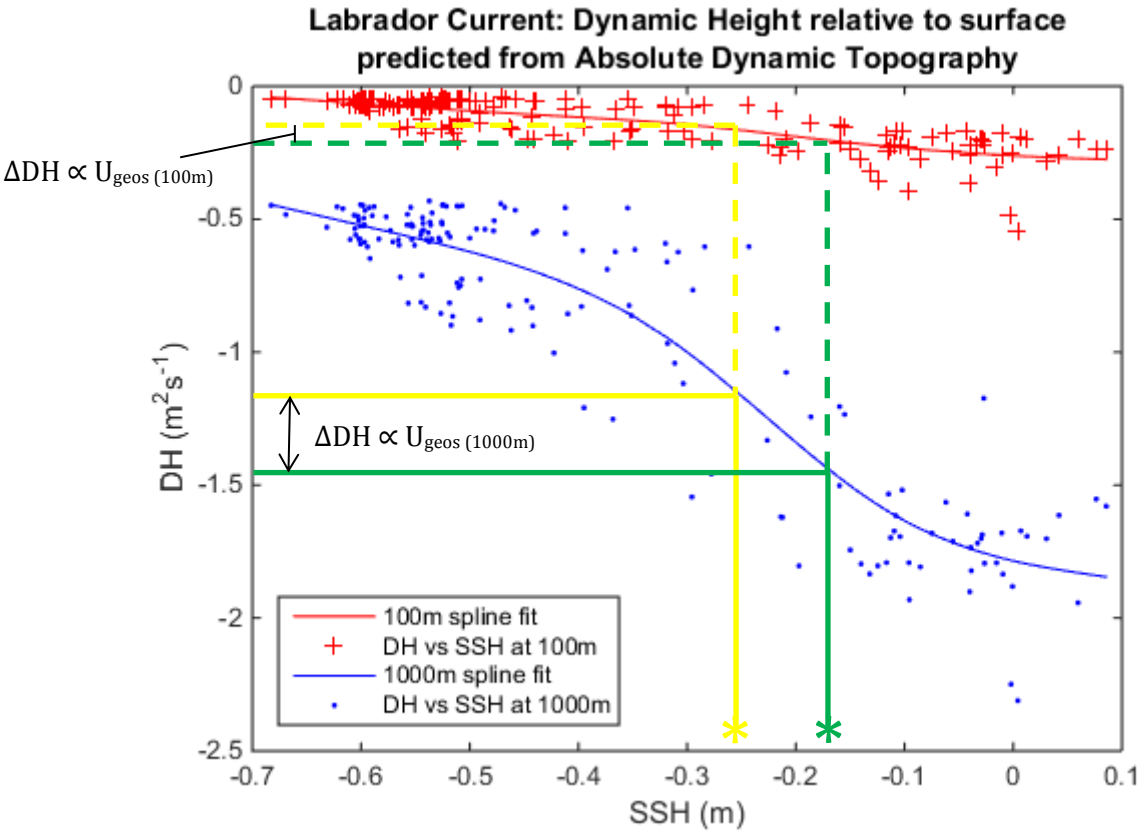

Figure 14b: The spline fits used to determine DH from SSH at the depths of 100m and 1000m (both relative to the surface) along the AR7W-North section. Green and yellow asterisks refer to upstream and downstream SSH measurements introduced in figure 14a.

Here we make the assumption that a robust DH-SSH relationship exists across the length of each transect, whilst also assuming that the relationship in the across-jet direction can be applied in the along-jet direction. Naveira Garabato et al (2011) make these same assumptions. The choice of an upstream and downstream distance of 500m is arbitrary. Whilst in theory this distance should be infinitesimally small, the choice to use 500m does not influence the resultant geostrophic velocities since it is a very small distance relative to the resolution of the SSH grid being interpolated.

5.4: Okubo-Weiss

Naveira Garabato et al (2011) found the Okubo-Weiss parameter *D* of the time mean flow to have some skill as a qualitative indicator of a jet's 'leakiness'. *D* is calculated as:

$$D = \frac{S_n^2 + S_n^2 - \Gamma^2}{4},$$

where $S_n = \frac{\partial u}{\partial x} - \frac{\partial v}{\partial y}$ is the normal component of rate of strain, $S_s = \frac{\partial v}{\partial x} + \frac{\partial u}{\partial y}$ is the shear component of the rate of strain and $\Gamma = \frac{\partial v}{\partial x} - \frac{\partial u}{\partial y}$ is the vertical component of the relative vorticity. This estimate of *D* is calculated from ADT-derived *u* and *v* for the LS (see figure 21).

5.5: Methodology Justifications

5.5.1: *Scale Separation*

If the tracer gradient associated with the mean flow in the LS is too abrupt, *equation (5)* cannot be applied. It is assumed that there is a scale separation between eddies and the mean flow, meaning that $|\Delta\theta_m/\Delta Y|$ must vary slowly over the duration of transects. It was expected that this assumption may be violated in the WGC where the topography is steepest and jets are most tightly constrained. In fact at mid-depths a more continuous gradient extends from WGC than the LC, from the boundary current to the centre of the LS (see figures 22a-b). This is possibly due to the strong signature of undiluted ISW in the deep WGC.

5.5.2: *Tracer fluctuations are generated by local stirring as opposed to advection*

Advection of tracer variance from regions upstream is assumed to be weak, and thus a negligible contribution to the θ_{RMS} term. In the LC it is suspected that the upstream Hudson Bay outflow contributes 50% of the FW budget of the LC, however this FW is trapped within the coastal LC and so imposes little on the tracer variability in the shelf break LC and deep LC (Straneo & Saucier, 2008). Observations by Myers et al. (2009) during June-July suggest that the WGC freshwater transport increases between Cape Farewell and Cape Desolation. Calculations by Myers et al. (2009) indicate that this transport increase is caused by active summer melting of Greenland glaciers. The anomaly is not statistically significant, however, and occurs between two moorings which do not enclose any glider or AR7W transect. In our current analysis we assume that contributions to tracer variance from Hudson Bay and Greenland glacial melt, as well as any other advected variability, are a negligible contributor to θ_{RMS} in the WGC and LC. Naveira Garabato et al. (2011) make a similar assumption in the ACC.

5.5.3: *Mixing is predominantly isopyncal*

Although eddy mixing is predominantly along isopycnals, diapycnal mixing in eddies is enhanced at the surface. For this reason, data above the mixed layer have been discarded before the calculation of L_{mix}. Various methods exist for calculation of mixed layer depth, however we

have made the assumption that the mixed layer depth is 60m throughout June-July, and 100m in May. Våge et al. (2008) identified the MLD in the LS to be a constant 60m from May-July with the exception of a few events in the first half of May, when some mixed layers approached 100m. This is only a precaution since it is commonly suspected that the general boundary current-interior exchange is caused by isopycnal mixing (Straneo, 2006), whilst the T-S modification of ISW around the LS basin can only be explained by isopycnal mixing, as opposed to diapycnal mixing (Cuny et al., 2002).

If the variability in tracer concentration about the mean is the product of lateral mixing, it should have a Gaussian distribution about the spline fit. After deleting data in the surface mixed layer, we find Conservative Temperature to have a strongly Gaussian distribution about the mean, with an average close to 0°C (-0.05°C), a standard deviation of 1.0039°C, a skewness of -0.47 and a kurtosis of 7.18. The histogram of the data distribution is plotted below, and the null hypothesis (that the data is of a non-standard distribution) is rejected by the Anderson-Darling normality test of the deviations.

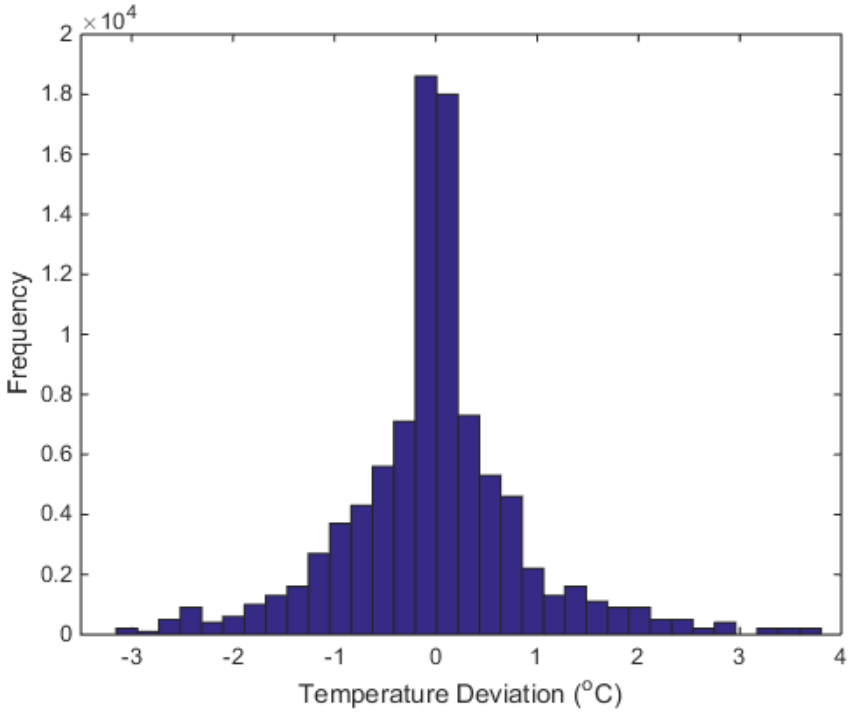

Figure 15: Conservative Temperature distribution about the spline fit for all AR7W data. The distribution is normal but strongly peaked.

Since the distribution about the spline fit is Gaussian, we argue that tracer variability is dominated by isopycnal mixing.

5.5.4: *Seasonal variability*

With respect to seasonal variability, only AR7W stations from the months May-July were included in the L_{mix} calculation in order to minimise seasonal tracer fluctuations. These months are outside of the convection period, during which Straneo (2006) find tracer changes in the central LS to reflect the vigorous lateral exchange with water masses from the boundary current. This observation would be supported by the strong variability in θ_{RMS}, which ranges from a maximum of ±4°C degrees in the WGC to a maximum of ±0.3°C in the centre of the LS (see figure 22d). With respect to winter deep convection, none of the seaglider transects presented in this report contain completely mixed profiles associated with Deep Convection. Deep convection is defined by a density difference of less than 0.01 kg m^{-3} between water at depth and at the base of the mixed layer (Frajka Williams et al., 2014). All glider transects included in this report are strongly and continuously stratified.

5.5.5: *Interannual Variability*

Within the WGC at Fylla Bank, timeseries show significant interannual variability during the months June-July alone, with long term means and standard deviations over 1950–2007 of 1.78±0.70°C and 33.41±0.25 for temperature and salinity respectively (Myers et al., 2009). Significant inter-annual variability has also been identified in models in both the fresh on-shelf component of the WGC and the salty off-shelf ISW component (Myers et al., 2009), whilst observations show significant variability in the shape and offshore position of the main shelf break front (Myers et al., 2009).

We therefore suspect that interannual variability may be a significant contributor to θ_{RMS}. Unusually weak convection has been observed in the central LS between the summer of 2005 until the spring of 2008, (Luo et al., 2012) and for this reason L_{mix} has been calculated for May/June of 2005-7 in order to obtain an estimate of θ_{RMS} with minimal contamination from interannual variability.

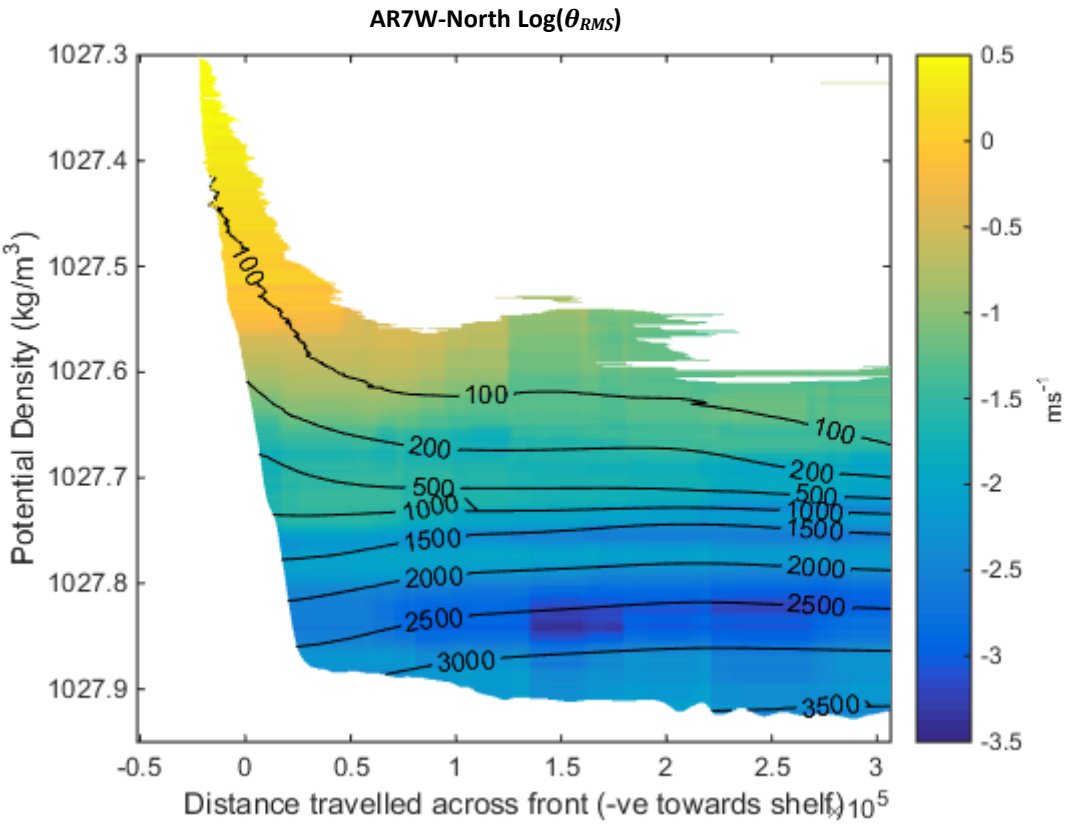

Figure 16: θ_{RMS} calculated across AR7W-North over the years 2005-7 for comparison with figure 22d.

Naveira Garabato et al (2011) find the calculation of L_{mix} converges when only using as few as 2 hydrographic section repeats, whilst L_{mix} variability occurs over scales of approximately 100km. The defining criterion is the requirement of 5-10 data points within the window ΔY, which is still fulfilled when only using 3 years of data, as there are commonly 6 data points within a 100km window which encompasses at least two stations worth of data at any one time. The calculated θ_{RMS} values are remarkably consistent when using either 3 years or 7 years of data, with an r^2 value of 0.995 (see figure 17). The relationship is particularly strong at high θ_{RMS} values.

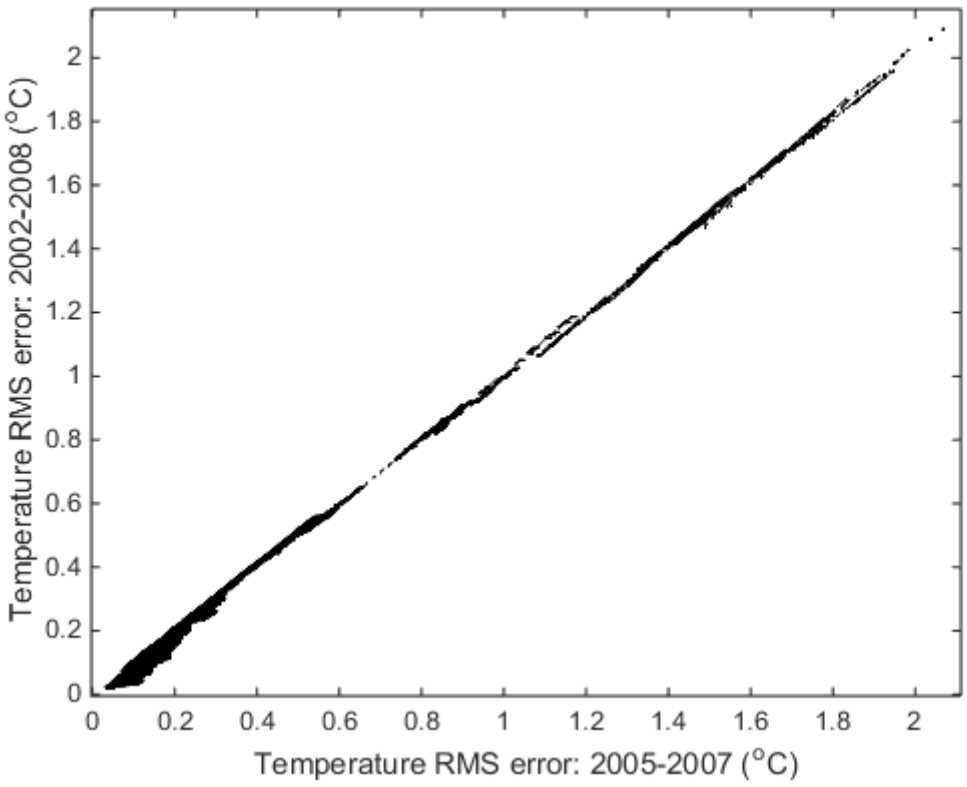

Figure 17: 2002-2008 θ_{RMS} plotted against 2005-2007 θ_{RMS} at equivalent isopycnals and cross frontal distance Y. The strong correlation suggests that θ_{RMS} changes very little when restricting the calculation to the years 2005-2007. R = 0.9985, p < 0.0001.

5.6: Parameter choice justifications

There are two main parameter choices that could be considered subjective. The rationale behind each choice is explained below.

5.6.1: *Conservative Temperature gradient: Computation of spline fit*

The choice of smoothing parameter for the L_{mix} calculation determines how much the $|\nabla_n \theta_m|$ term reflects the basin scale gradient versus the local gradient. Ideally the gradient should be as linear as possible, whilst still being representative of the mean θ at each station (in the case of the AR7W transects). The choice of a spline fit smoothness is inevitably subjective, however it was ensured that the chosen spline fit was both: firstly monotonic at all depths and, secondly, approximately representative of mean tracer concentrations at each station. This meant selecting spline fits which were as rough as possible but which still remained monotonic towards the centre of the LS.

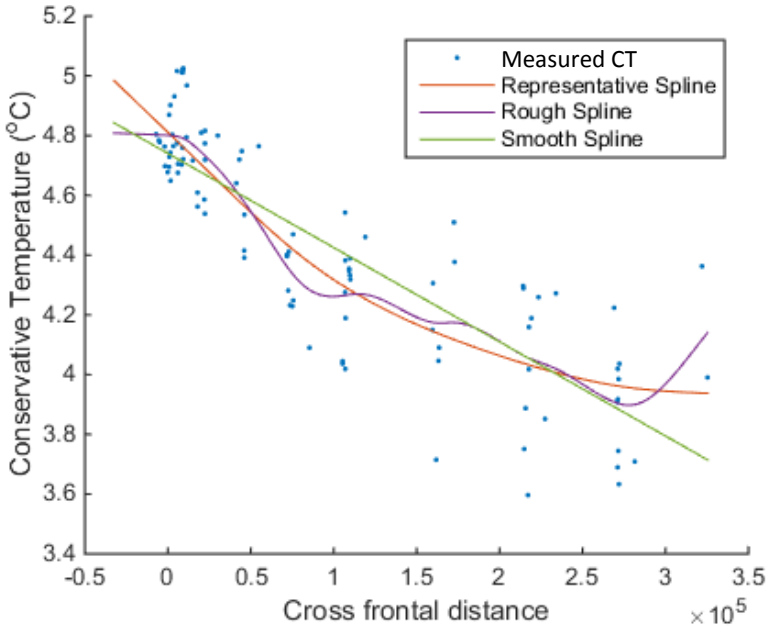

Figure 18: Conservative temperature on ρ_θ = 1027.7 kg m^{-3} along AR7W-North. Spline fits are chosen to be as rough as possible whilst staying monotonic.

On some isopycnals, a representative spline fit identifies in an extremely small gradient, and the resulting L_{mix} is extremely large. In a similar manner to Naveira Garabato et al. (2011), we have removed eddy mixing lengths over 350km before using L_{mix} for further analysis. This distance is an appropriate maximum for L_{mix} in the LS, as it is the largest distance to the core of either boundary current across the AR7W section.

5.6.2: *θ_{RMS} calculation: window size ΔY*

The calculation of L_{mix} involves the subjective choice of a distance interval ΔY encompassing a range of data from which to calculate θ_{RMS}. As for Naveira Garabato et al (2011), our choice of ΔY is guided by the requirement of at least 5-10 data points within the window. For the AR7W transects, a window with a full width of 100km, approximately twice the widest station spacing, was employed in order to continuously encompass at least two stations worth of data within the window at all times. Increasing this window to 150km in order to continuously encompass three stations only acts to blur out any identified maxima in θ_{RMS}, whilst using a window of 30km and only one station worth of data caused the θ_{RMS} field to be undesirably noisy. Any choice of ΔY approximately encompassing a distance equivalent to 2 stations (100-130 km) was found to have a negligible effect on the resultant L_{mix} magnitude at any location (<5%).

6: Results

6.1: Preliminary Results: ADT-derived results

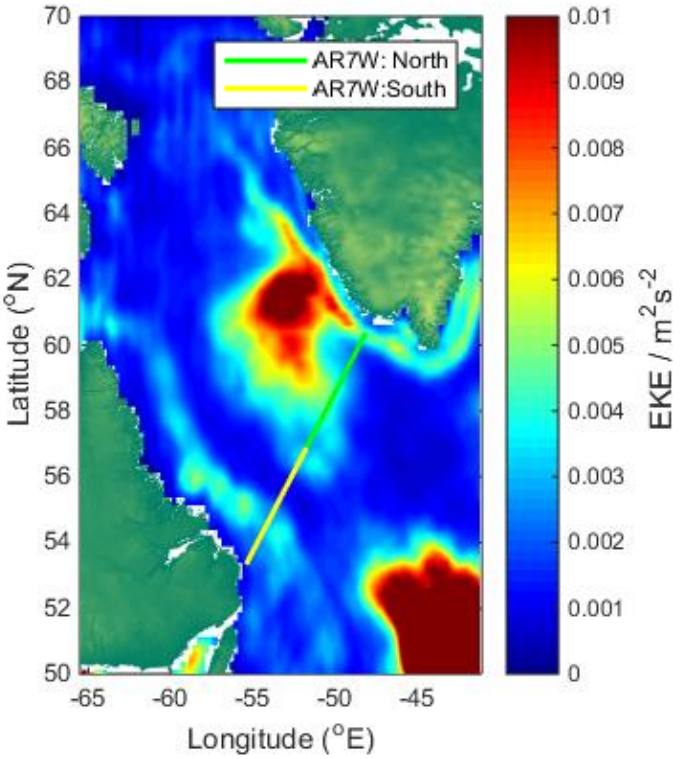

Figure 19a: EKE in the LS. EKE is highest in the Centre-North LS. There is also high EKE in the Northern WGC and a small amount of EKE in the LC. Altimeter data artefacts exist in the North-West LS.

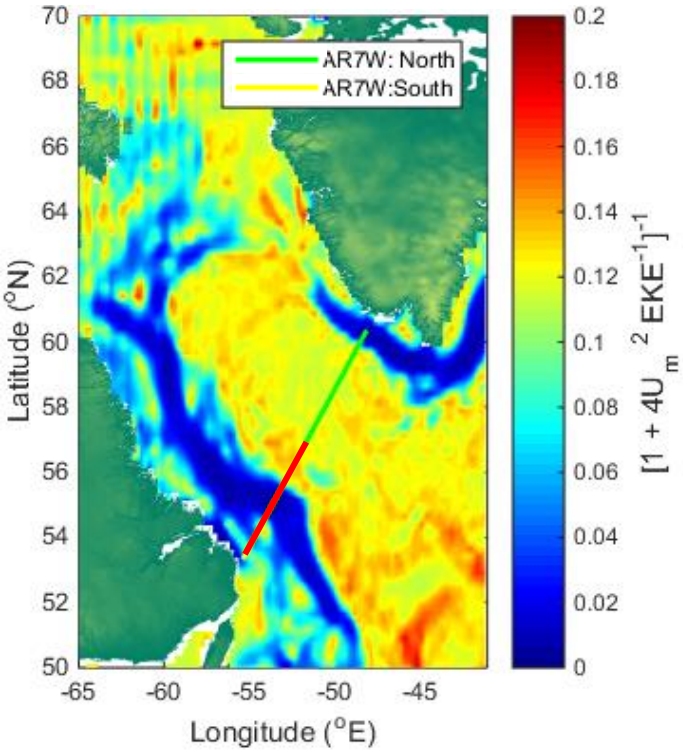

Figure 19b: The ISF $(1 + 4U_m^2 EKE^{-1})^{-1}$ in the LS. The ISF suggests suppression in both the LC and WGC but possibly more extensive suppression in the shelf break and deep LC. Altimeter data artefacts exist in the North-West LS.

Calculations of the ADT-derived inverse suppression factor (ISF) $(1 + 4U_m^2 EKE^{-1})^{-1}$ find the EKE within the boundary currents to be lower than expected from the mean flow field. The entire LC and WGC appears to be suppressed, with the exception of some of the Northern WGC. As is widely known, figure 19a finds enhanced EKE in the boundary currents and in a patch in the central LS originating from the WGC. Since eddies do form in the LC and WGC, the shortfall in EKE indicated by figure 19b could be interpreted as a genuine feature. In the bifurcated current between the WGC and LC, there is a shortfall in EKE indicated by figure 19b, however the complete absence of any eddy activity here (see figure 19a) would suggest that suppression may not be occurring. Rather, the EKE 'shortfall' in these recirculation cells simply reflects the complete lack of instabilities here.

Conversely, the Okubo-Weiss parameter *D* of the mean flow surface suggests that suppression is not the dominant regime, as the mean flow field has patches of divergence and convergence equal or greater in magnitude to those seen in the 'leaky jet' segments identified the ACC by Naveira Garabato et al. (2011). As is apparent in the ISF (in figure 19b), these regions of high magnitude *D* are limited to the WGC and LC but are not found in the Northern WGC. The leaky jets in question in the ACC are at an approximately equivalent latitude in the Southern Hemisphere, meaning values of *D* in the LS should be directly comparable to the ACC.

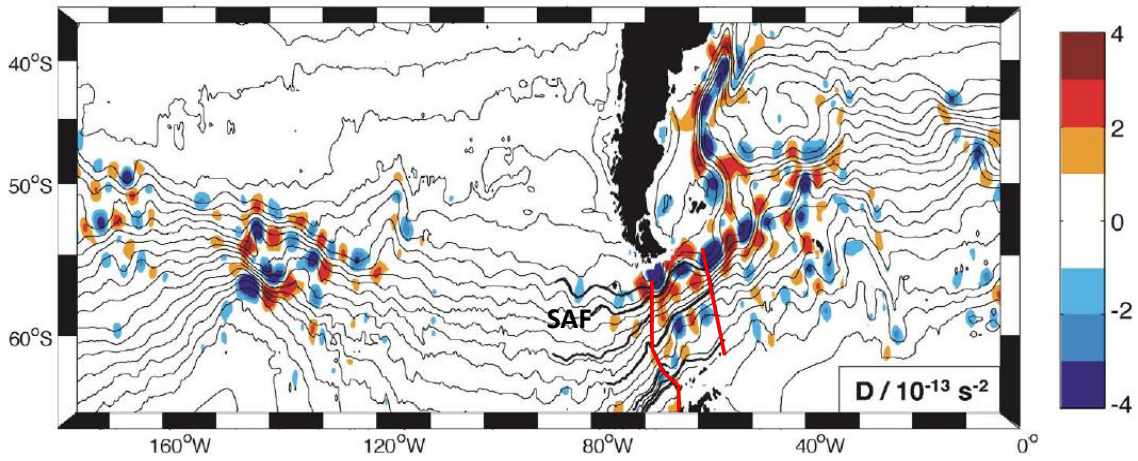

Figure 20: Okubo-Weiss parameter *D* over a section of the ACC: a modification of figure 2e from Naveira Garabato et al. (2011). Red lines are WOCE transects, and thick black contours are ACC jets. The SAF Jet (labelled) becomes leaky across Drake Passage at the tip of South America, as indicated by increased Okubo-Weiss parameter magnitudes.

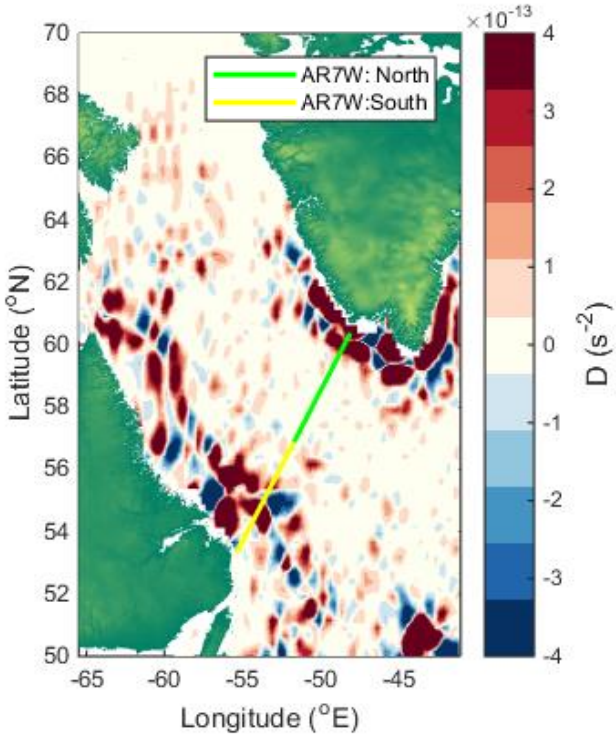

Figure 21: Okubo-Weiss parameter *D* in the LS (plotted above) is comparable in magnitude to that of *D* in the ACC.

6.2: Mixing length analysis results

An important limitation of our findings here is that the tracer diffusivity does not translate to buoyancy diffusivity in the LS. The vertical structure of the potential vorticity (PV) diffusivity and thus the diffusivity of tracers is strongly depth-dependent, whereas buoyancy diffusivity often shows less of a vertical structure (Smith and Marshall, 2009). PV diffusivity does however reflect the mixing properties of the flow more appropriately than buoyancy diffusivity, however, and can be used to calculate the buoyancy diffusivity provided the Coriolis parameter, planetary vorticity gradient and vertical tracer gradient is known (Smith and Marshall, 2009).

Since the LS exhibits interannual variability in EKE (Eden & Böning, 2002), the following results only represent the mixing regime over the years 2002-2008. Results are also only representative of the part of the boundary current that the AR7W transect crosses, and may not extrapolate to the rest of the boundary current.

The strong continuous tracer gradient extending from the WGC can be seen clearly in figure 22b, and is strongest at about 200m depth. It is generally well defined down to approximately 2000m. The tracer gradient $|\nabla_n \theta_m|$ extending from the LC is weaker, with useable gradients between approximately 200-1000m and 1500-2000m. In both halves of the AR7W transect, the gradient in the central LS is effectively zero, rendering any L_{mix} results in this region invalid. An approximate anti-correlation exists between tracer θ_{RMS} and $|\nabla_n \theta_m|$. The resultant L_{mix} field is predominantly a reflection of $|\nabla_n \theta_m|$, as θ_{RMS} is relatively unvarying across any one isopycnal.

U_{eddy} is found to be relatively constant with depth, and generally reflects the surface EKE field (see figure 19a). Also apparent are defined minima in U_{eddy} offshore of the boundary currents, and a far less pronounced U_{eddy} maximum within WGC than the LC. Estimates of kc_e^{-1} are predominantly a reflection of L_{mix}, however in the LC at Y=0 a maximum in U_{eddy} translates to a maximum in kc_e^{-1}.

Labrador Current **Western Greenland Current**

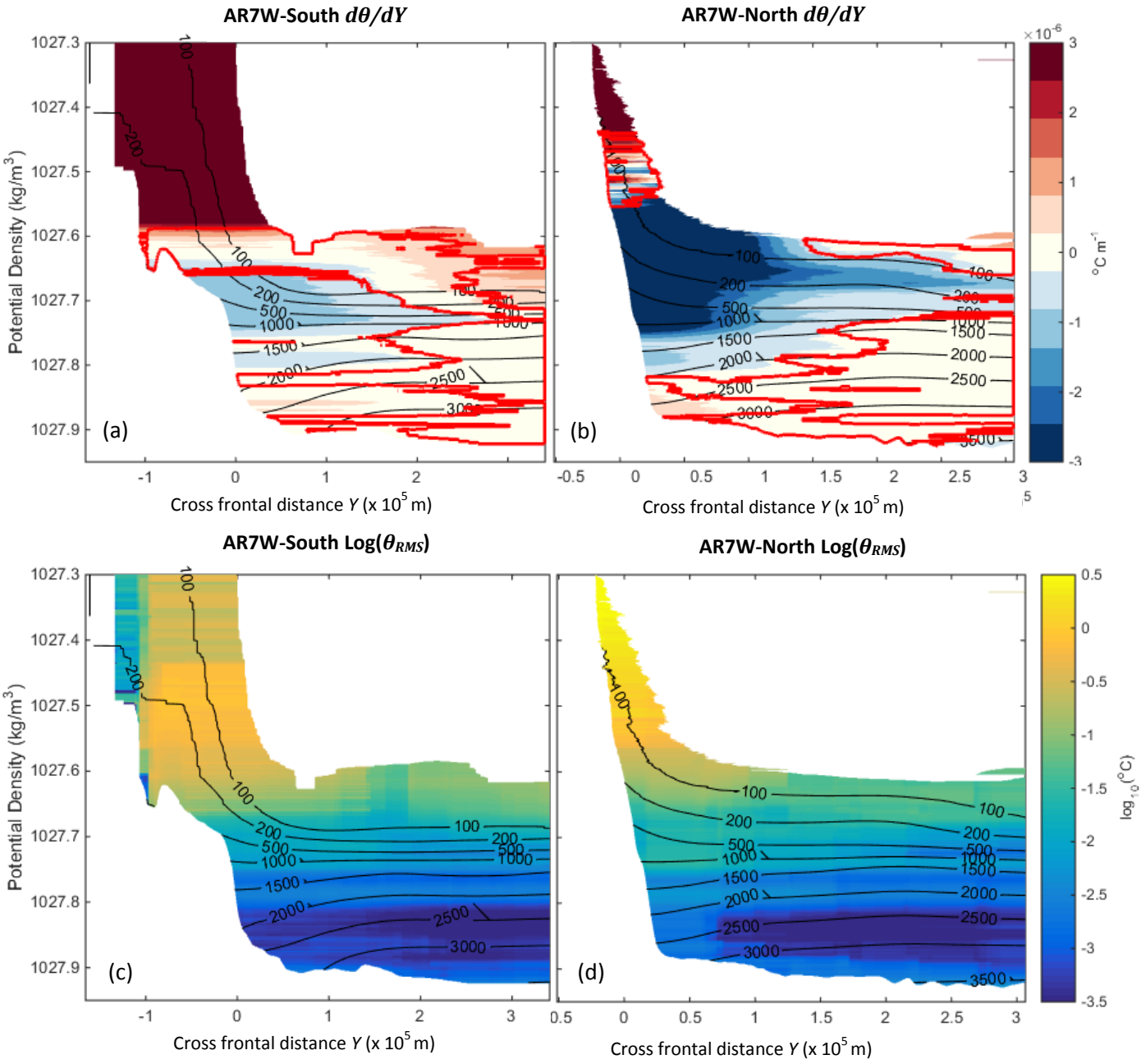

Figures 22 a-d: CT gradient $\nabla_n \theta_m$ (a-b) and $\log_{10}$ of θ_{RMS} in CT (c-d) at each isopycnal along AR7W-South and AR7W-North. Cross frontal distance Y is positive offshore. Red lines enclose regions where the mixing length is greater than 350km. Black contours are bin averages of the depth at which each isopycnal lies.

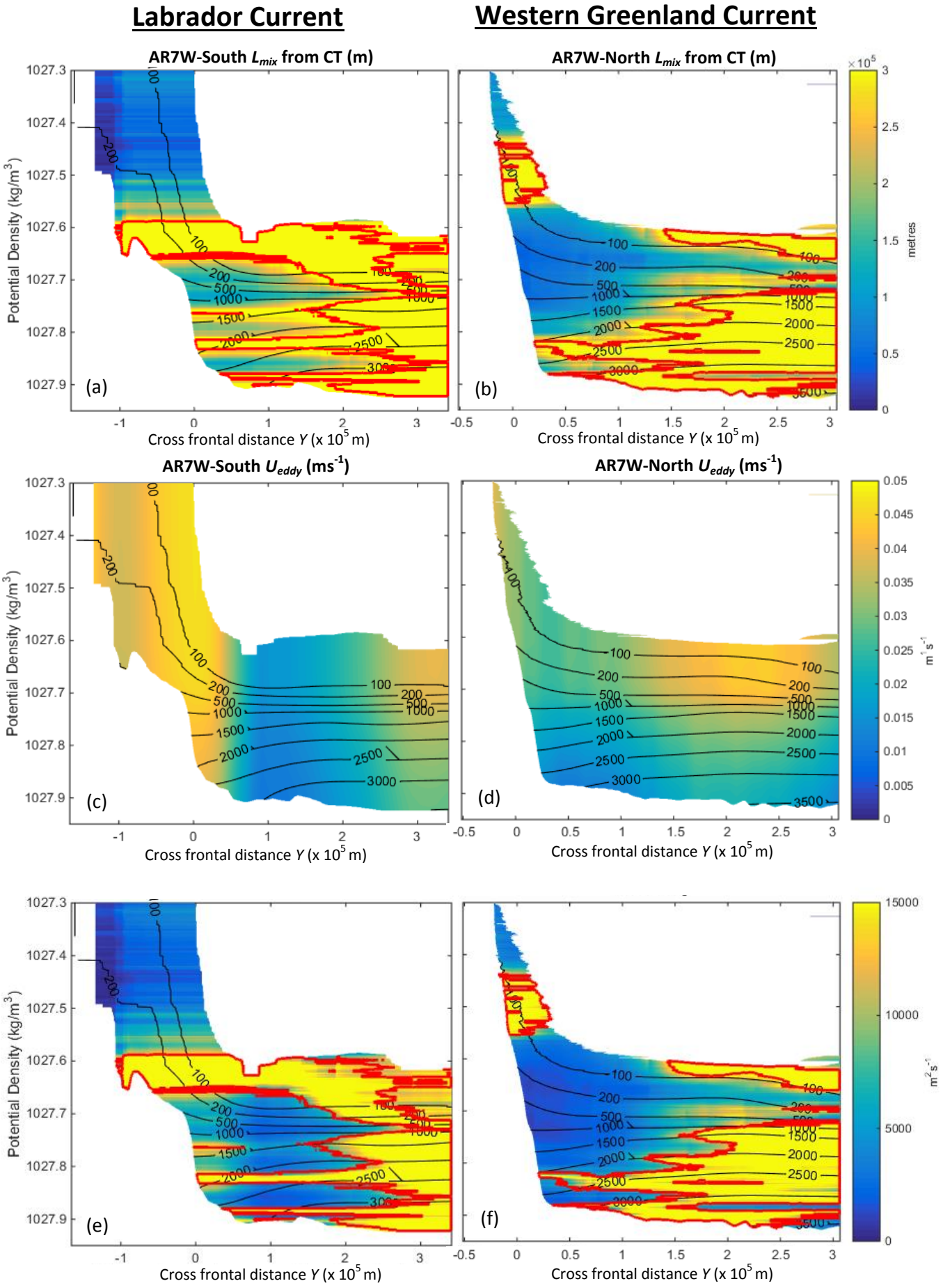

Figures 23 a-f: Mixing length L_{mix} (a-b), across-jet eddy velocity scale U_{eddy} (c-d) and relative eddy diffusivity kc_e^{-1} (e-f) at each isopycnal along AR7W-South and AR7W-North. Cross frontal distance Y is positive offshore. Red lines enclose regions where the mixing length is greater than 350km Black contours are bin averages of the depth at which each isopycnal lies.

Figures 25 and 27 explore relationships between the derived variables. In figures 24c-d and 26c-d, depth-weighted kc_e^{-1} and L_{mix} averages include data for which L_{mix} < 350km. Note in some regions, this depth average may only reflect mixing lengths and eddy diffusivities over a narrow range of isopycnals.

Depth averages of L_{mix} and kc_e^{-1}, identify a clear L_{mix} and kc_e^{-1} minimum in AR7W-North at Y=0, i.e. in the core of the WGC. In AR7W-South, however, there is no clear minimum in L_{mix} at Y=0; in fact kc_e^{-1} is at a maximum at Y=0 due to the particularly high U_{eddy} on the shelf (see figure 23d). The lack of a clear minimum or maximum in L_{mix} may be due to the very select range of valid depths over which the depth-average is obtained.

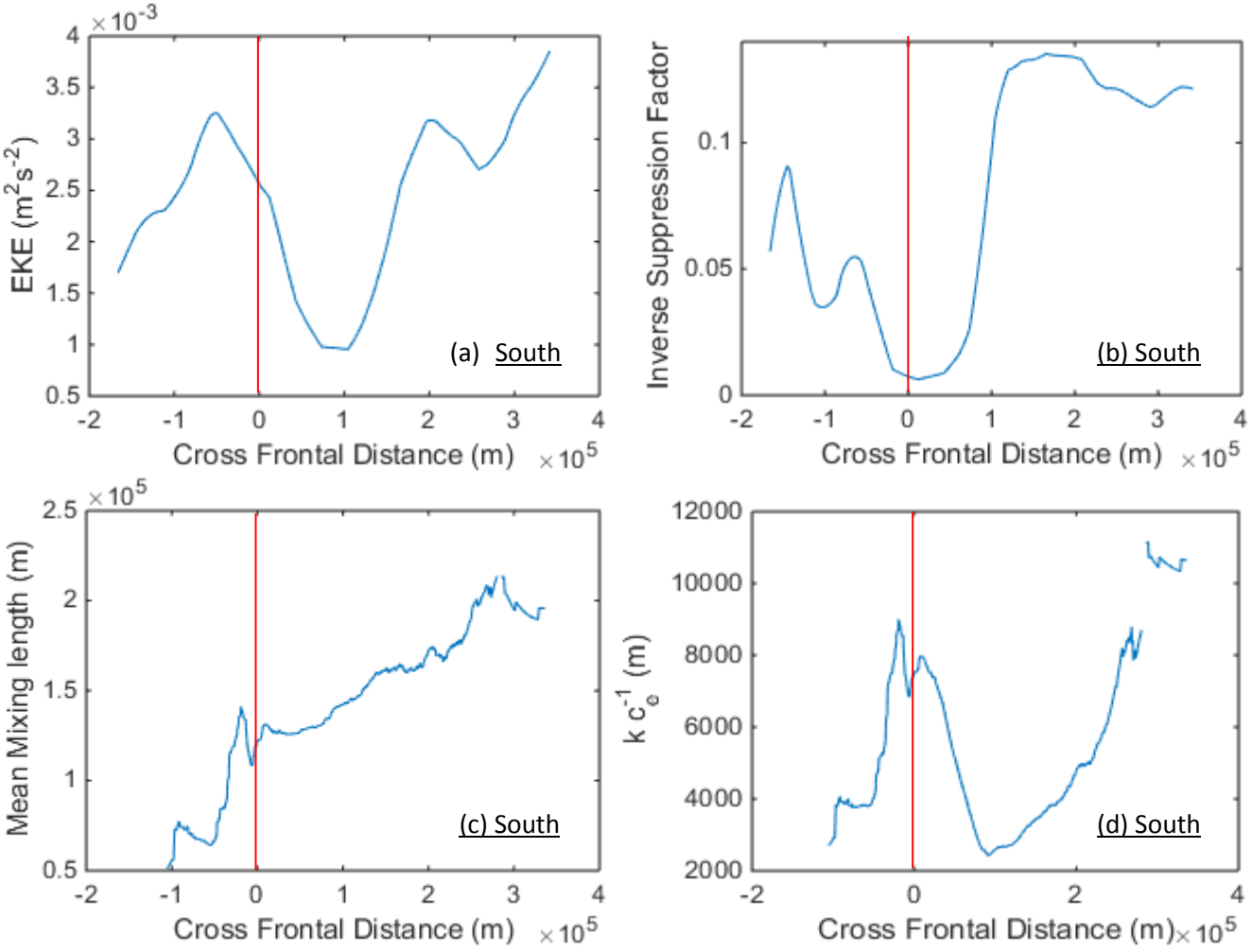

Figures 24 a-d: (a) EKE, (b) Inverse suppression Factor, (c) depth averaged L_{mix} and (d) depth averaged kc_e^{-1} along AR7W-South. Red lines mark Y=0.

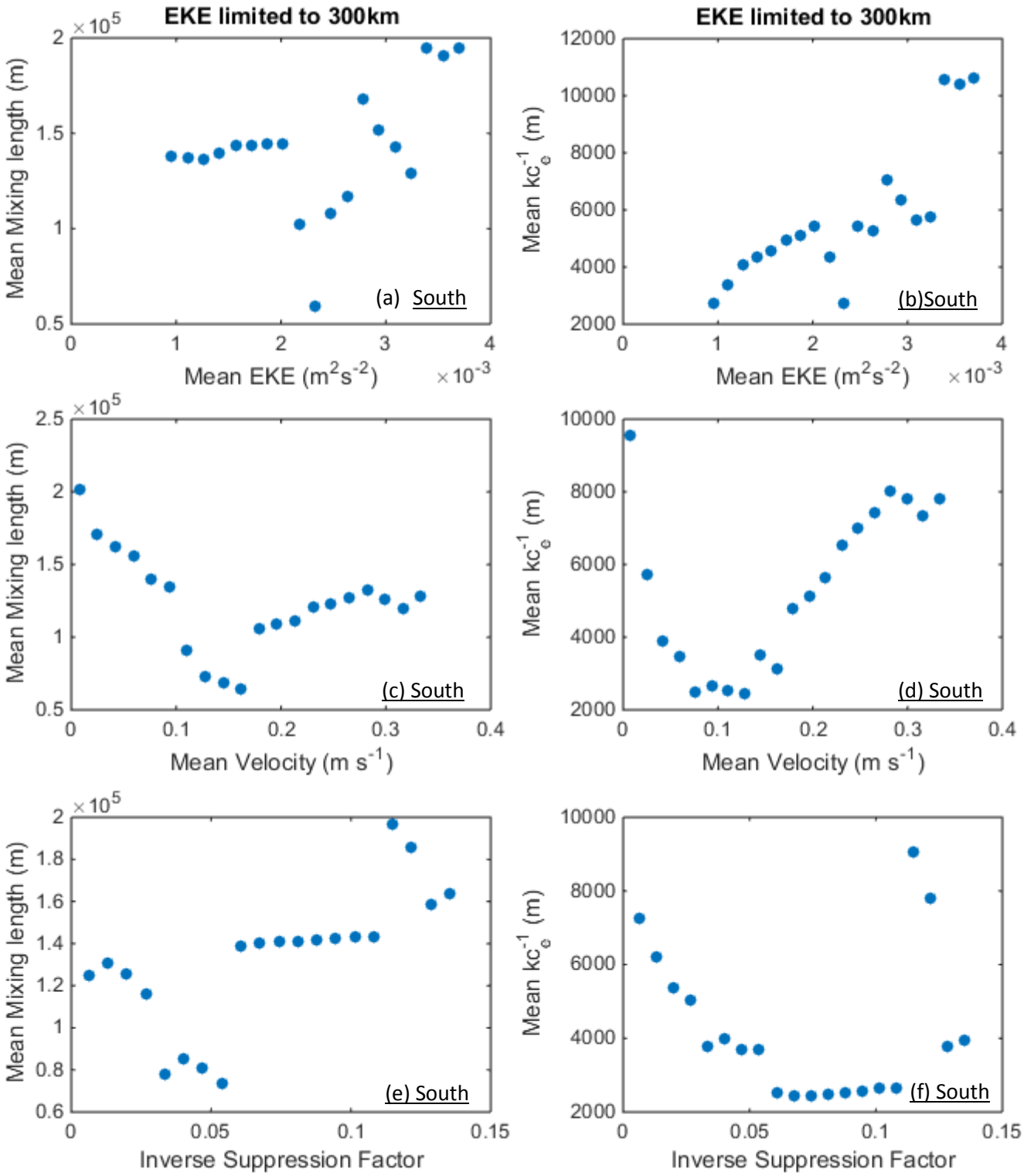

Figures 25 a-f: (a) Mean L_{mix} bin averaged onto surface mean EKE, (b) Mean kc_e^{-1}bin averaged onto surface mean EKE, (c) Mean L_{mix} bin averaged onto U_{mean}, (d) Mean kc_e^{-1}bin averaged onto U_{mean}, (e) Mean L_{mix} bin averaged onto inverse suppression factor and (f) Mean kc_e^{-1}bin averaged onto inverse suppression factor along AR7W-South. Bins are all 1/20th of the range of the variable plotted on the x axis. Pearson's correlation coefficient R- and p-values are as follows: (a) R = 0.4012, p = 0.0886 (b) 0.8162, p < 0.0001 (c) R = -0.3599, p = 0.1190 (d) R = 0.5083, p = 0.0221 (e) R= 0.6946, p = 0.0007 (f) R = -0.1190, p = 0.6173.

Across AR7W-South, the ISF is at an approximate minimum at Y=0 (see figure 24b), whereas EKE is closer to a maximum than at Y=0 (see figure 24a). Naveira Garabato et al. (2011) identify a predictable inverse relationship between L_{mix} and mean current velocity (U_{mean}), as well as a strong linear relationship between L_{mix} and the ISF. Only jets identified as 'leaky' were found to deviate from these relationships. In the LS, no strong correlations exist between either L_{mix} and U_{mean}, or L_{mix} and the ISF. Rather than a well-defined relationship, in both the WGC and the LC the relationship between the mean flow velocity and L_{mix} or kc_e^{-1} is relatively u-shaped, with a minimum in L_{mix} or kc_e^{-1} at 0.1-0.2 ms^{-1}. There also tends to be a poorly defined minimum in L_{mix} and kc_e^{-1} at ISF = 0.05. A strong relationship does exist, however, between surface EKE and L_{mix} as well as between EKE and kc_e^{-1} in the WGC (see figure 27a-b).

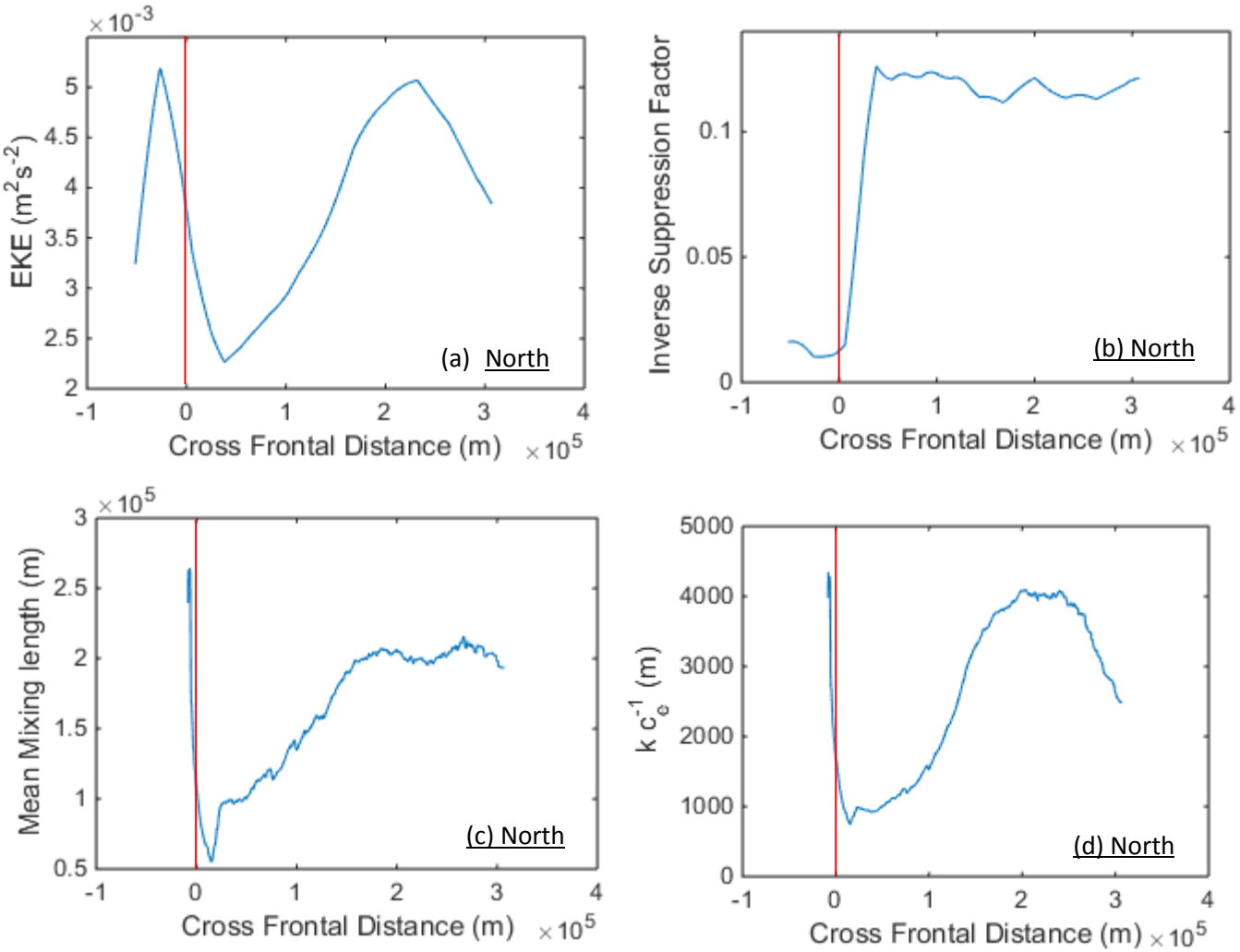

Figures 26 a-d: (a) EKE, (b) Inverse suppression Factor, (c) depth averaged L_{mix} and (d) depth averaged kc_e^{-1} along AR7W-North. Red lines mark Y=0. Abrupt peak in figures c-d are due to very few useable data points at Y<0.

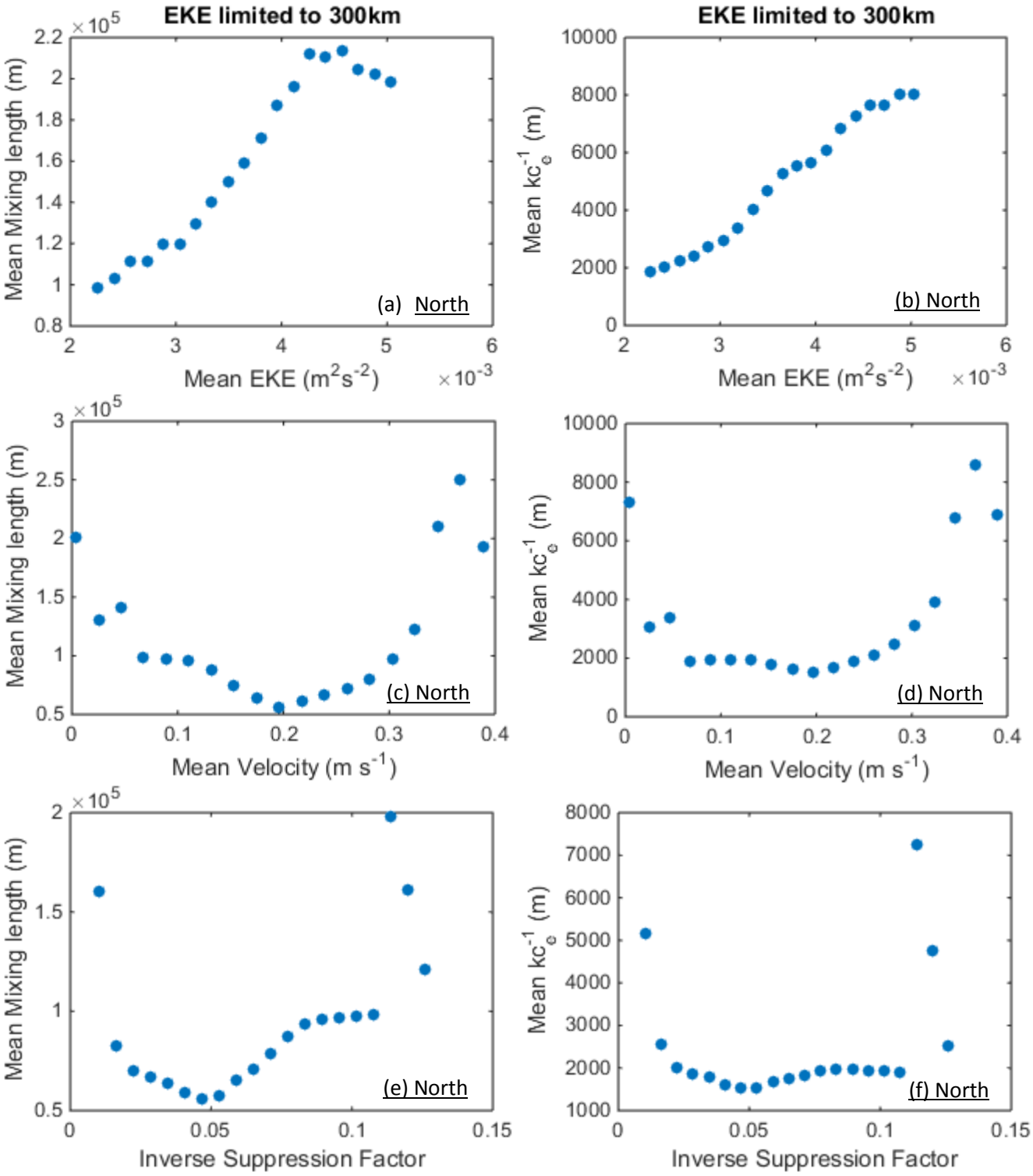

Figures 27 a-f: (a) Mean L_{mix} bin averaged onto surface mean EKE, (b) Mean kc_e^{-1}bin averaged onto surface mean EKE, (c) Mean L_{mix} bin averaged onto U_{mean}, (d) Mean kc_e^{-1} bin averaged onto U_{mean}, ,(e) Mean L_{mix} bin averaged onto inverse suppression factor and (f) Mean kc_e^{-1}bin averaged onto inverse suppression factor along AR7W-North. Bins are all 1/20th of the range of the variable plotted on the x axis. Pearson's correlation coefficient R- and p-values are as follows: (a) R = 0.9598, p < 0.0001 (b) 0.9918, p < 0.0001 (c) R = 0.2363, p = 0.3300 (d) R = 0.3681, p = 0.1210 (e) R = 0.4769, p = 0.0335 (f) R = 0.2293, p = 0.3309.

6.3: Glider-derived diffusivities

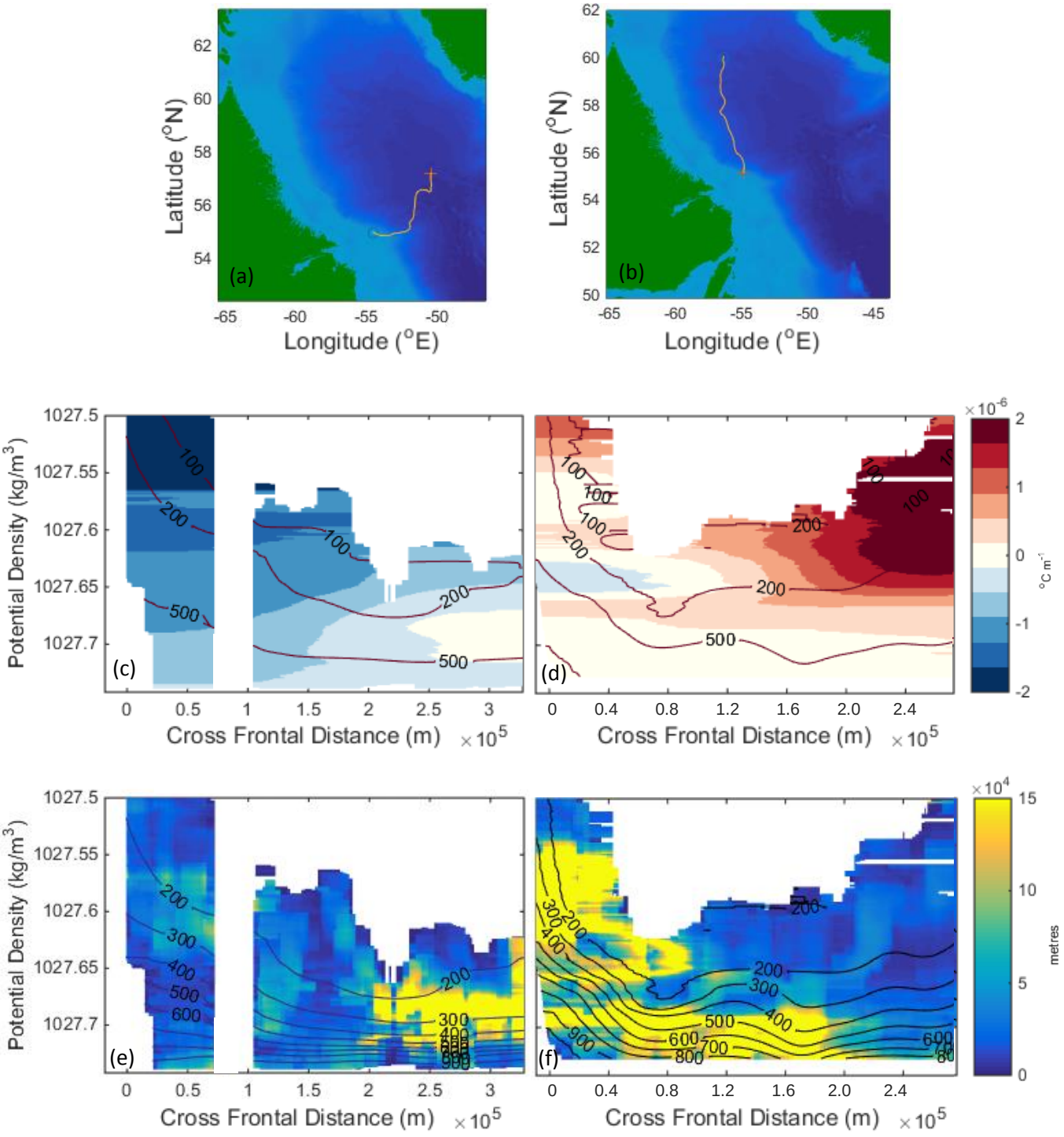

Figures 28 a-f: (a) Location of transect 14d, (b) Location of transect 7c (c) Temperature gradient across transect 14d (d) Temperature gradient across transect 7c (e) L_{mix} across transect 14d and (f) L_{mix} across transect 7c. Mapped glider transects terminate at the end demarked with a +. Black contours are bin averages of the depth at which each isopycnal lies. Transect 14d was taken by seaglider 004 from Dec 2004-Jan 2005 and transect 7c was taken by seaglider 014 in Jan 2004.

Whilst some glider transects produced reasonable results, most transects cross the LC, and only offered tracer gradients that were not monotonic. A minority of glider transects had sufficiently strong and continuous gradients to obtain mixing length estimates. As examples, we include the location, temperature gradient and mixing lengths for two glider transects. Transect 14d is the most successful transect, showing a strong CT gradient stemming from the LC (see figure 28c) and finding a relatively constant mixing length within 150km of the LC. In transect 7c, however, the glider travels northwards and finds a more convoluted temperature gradient (see figure 28d) and resultant L_{mix} field. Due to the strong latitudinal variability in tracer gradients, L_{mix} derived from glider transects shows no pattern or structure, and for this reason glider data does not feature heavily in the results included here. It is suspected that some of the glider transects may provide a relatively instantaneous estimate of L_{mix}.

7: Discussion

As mentioned in section 6.1, calculations of D indicate that both the WGC and LC are leaky, whilst the ISF reveals a shortfall in the EKE within these currents, suggesting that suppression may be occurring. One potential drawback of the ISF is that it is based on *equation (2)*, an empirical equation which applies to the ACC. Since the LS and ACC are both at a similar distance from the equator, the Rossby radius of deformation in the LS will be similar to the, however the empirical relationship in *equation (2)* will vary depending on geographical location and the local eddy propagation speeds relative to the mean flow. It must be considered that the apparent 'shortfall' in EKE indicated by the ISF may relate to the unsuitable use of this equation. Since satellite evidence from the ISF and D yields two conflicting arguments, we seek clarification from in situ estimates of diffusivity.

7.1: AR7W-North: Unsuppressed mixing

Looking to the calculated L_{mix} and kc_e^{-1} in AR7W-North, the first prominent feature is that minima in L_{mix} and kc_e^{-1} exist approximately at Y=0. These minima are found to be robust features which exist even when data for which L_{mix}>150 km is excluded from the depth-averaging. Whilst no minimum is seen in the calculated U_{eddy}, there is no intensification in U_{eddy} at Y=0 (see figure 23e) for AR7W-North. We argue below that the minima in L_{mix} and kc_e^{-1} at Y=0 may not necessarily mean that mixing is being suppressed in the sense that the WGC is forming a barrier to eddies.

Naveira Garabato et al. (2011) identify a strong linear relationship between L_{mix} and the ISF in mixing-suppressed fronts of the ACC. Neither over AR7W-North or AR7W-South does a linear relationship exist between the ISF and kc_e^{-1} or the ISF and L_{mix}. A very strong linear relationship is, however identified between EKE and kc_e^{-1} as well as between EKE and L_{mix} in the WGC. This would suggest that despite reduced L_{mix} and kc_e^{-1} in the WGC, suppression is not the dominant regime. Instead, L_{mix} and kc_e^{-1} minima in the WGC simply reflect the surface EKE minimum near Y=0; AR7W-North passes through a relatively laminar section of the WCG where the current rarely forms instabilities and the mean EKE is abnormally low (see figure 19a). Furthermore, contrary to the case in the ACC, maxima in U_{eddy} and L_{mix} are approximately coincidental in

AR7W-North. In suppressed fronts of the ACC, maxima in U_{eddy} were associated with minima in L_{mix}.

It could be argued that since the ISF is tailored to the ACC and not the LS, the lack of a linear correlation between L_{mix} and ISF is unsurprising, and that the factor is incompatible with the LS because the empirical relation places too much or too little emphasis on EKE in the EKE-U_{mean} relationship. Even in this case, some correlation would still be expected (linear or otherwise) between kc_e^{-1} and the ISF, whereas we find no relationship of any kind in the LS.

It should also be acknowledged that the EKE-L_{mix} relationship across AR7W-North breaks down at higher EKE values, as would be expected in a suppressed regime. It would be incorrect to interpret this as suppression, however, as the highest EKE bins used in the bin-averaging originate from nearer the central LS rather than from within the WGC core (see AR7W-North in figure 19a).

7.2: AR7W-South: Poor tracer gradient

In AR7W-South, whilst there is no clear maximum or minimum in L_{mix}, a maximum in U_{eddy} translates to a broad peak in kc_e^{-1} in the core of the LC. No strong correlations exist between any of the derived variables.

Our estimates of depth averaged L_{mix}, and subsequently kc_e^{-1}, are larger in the LC than in the WGC. The unexpected implication here is that mixing is actually stronger in the LC than the faster-flowing WGC. It is unexpected that eddy mixing is stronger in the LC than the WGC: previous research finds that due to the weaker eddy mixing in the LC, 60% of the seasonal FW comes from the WGC boundary current (Schmidt & Send, 2007) whilst only 6-8% of the FW exported from the Canadian Arctic actually enters the LS via the LC (Myers, 2005). Furthermore L_{mix} calculated across glider transect 14d also compare badly with AR7W-South. We therefore conclude that the higher mean L_{mix} (and the lack of any strong correlations in figures 25a-f) across AR7W-South is most likely because there is a very select range of depths over which L_{mix} < 350km in AR7W-South. When a threshold much lower than 350km is used as the maximum acceptable resultant L_{mix}, large amounts of the AR7W-South transect are disposed of, meaning

the tracer gradient is fundamentally too weak for the majority of AR7W-South to definitively characterise the mixing regime across the LC. It would be erroneous to trust the high kc_e^{-1} values calculated across AR7W-South.

7.3: Mixing time estimate

From kc_e^{-1}, characteristic time scales can be established to describe the mixing of tracers from the boundary currents.

Although kc_e^{-1} is highly variable with depth, the depth-averaged value of kc_e^{-1} in the core of the WGC is approximately 1000 $m^2\ s^{-1}$, with maximum eddy diffusivities of up to 4000 $m^2\ s^{-1}$ in the centre of the LS in AR7W-North. Since the poor tracer gradient in AR7W-South yields poor depth-averages of kc_e^{-1} in the LC, we will take 1000 $m^2 s^{-1}$ to be the representative eddy diffusivity of both boundary currents in the following calculation.

Since the shelf-break boundary currents are approximately 80km-120km wide (see figure 8), an appropriate distance scale from the core of these currents to the LS interior would be 50km. In the absence of a better estimate of c_e in the LS, we use the quasi-global mean mixing efficiency of c_e = 0.16 of Wunsch (1999), yielding a value of k = 160 $m^2\ s^{-1}$.

In terms of a mixing timescale for a parcel of water circulating the LS in a boundary current, time t taken for mixing into the central LS is:

$$t = L^2/k = (50\ 000)^2/160 = 6\ 250\ 000 \text{ seconds, or } 4.8 \text{ years.}$$

Cuny et al. (2002) find the boundary currents to have a mean transit time from the tip of Greenland to the South LC at 50°N of 310 days, a short timescale relative to 4.8 years. This suggests that limited mixing occurs in the boundary currents, consistent with observations that the majority of deep boundary current modification occurs during the diffuse circulation from the WGC to the LC (Cuny et al., 2002). Still, it should be recognised that this mixing time is based entirely on a single transect through the WGC, at a location where the WGC is abnormally stable. In reality, mixing will be enhanced at points where instabilities frequently develop.

7.4: Implications of results

7.4.1: *Implications for IRs, CEs and BCEs*

The relative importance of IRs, CEs and BCEs is still contested. IRs are known to transport large volumes of stratified water from the WGC into the LS, preventing deep convection from occurring above approximately 58°N (Chanut et al., 2008). They induce smaller eddies and are effective mixers, contributing approximately 45% to the seasonal buoyancy forcing of LS. Comparatively, both CEs and BCEs contribute approximately only 30% (Gelderloos et al., 2011). The dominant convection-inhibiting effect of IRs, combined with strong interannual variability in WGC and Irminger Current (IC) instability (Eden & Böning, 2002) means that these eddies could modulate interannual variability in LSW formation and AMOC circulation (Chanut et al., 2008).

At the point where AR7W-North intersects the WGC, BCEs will be formed. Further downstream of AR7W-North the WGC becomes more unstable and forms IR instabilities. Our findings suggest that mixing by BCEs in the WGC is unsuppressed, and whilst it would follow that the WGC becomes more 'leaky' downstream of AR7W-North, the interaction of the mean current with IRs may be different. It would therefore be premature to assume the entirety of the WGC is unsuppressed, however due to their relative contributions to the LS buoyancy budget we suspect that mixing by IRs is less likely to be suppressed than mixing by BCEs.

7.4.2: *Implications for the AMOC*

Returning to the wider context, unsuppressed eddy mixing could potentially have dire consequences for the AMOC, depending on whether two AMOC equilibria can exist under the same conditions. This is known as bistability, and the question of whether the AMOC is bistable or not depends on whether the AMOC imports or exports FW. If the AMOC exports freshwater, a freshwater perturbation from the LS boundary currents could disrupt the current day delicate positive feedback cycle (Kuhlbrodt et al., 2007).

Current observations suggest an overall AMOC FW transport between -0.2 and +0.05 Sv (Dansgaard et al., 1993), meaning we are unable to resolve the boundary between FW import or export. Our interpretation of unsuppressed mixing in the AR7W-North will only be of severe consequence in the case that firstly this finding extrapolates to the rest of the WGC, and that secondly the AMOC is indeed bistable. Unfortunately we still do not know whether either of these conditions apply.

7.4.3: *Implications for satellite-based studies*

In the case that the unsuppressed regime at AR7W-North applies to the rest of the LS, EKE in the LS may prove to be an extremely useful indicator of kc_e^{-1}. With validation from further in situ mixing-length studies, an altimeter based method could even be used to quantify accurate tracer transports out of the boundary currents.

8: Conclusions

The results of this study are limited by the magnitude of tracer gradients along some isopycnal surfaces in the LS, meaning dependable results have only been obtained for AR7W-North. Neither AR7W-South or glider-derived diffusivities are found to be reliable, meaning we can neither support nor refute **hypothesis 1** (see page 10). With respect to **hypothesis 2** (see page 15), whilst eddy diffusivity seems to be unsuppressed in the core of the WGC, we have not been able to obtain any such results for the LC.

This study provides a first platform upon which to study the suppression of eddy mixing in the LS. Our primary finding is that of the reduced kc_e^{-1} within the WGC relative to the surroundings. This has not been interpreted as suppression of mixing by the front, since kc_e^{-1} shares no relationship with the ISF. We tentatively conclude that suppression may not be the dominant regime in the WGC, based on the informed observation of a single unusually stable cross-section of the WGC, whilst assuming that the WGC becomes more 'leaky' downstream of AR7W-North. This study also finds the surface EKE to be a viable predictor of kc_e^{-1} and L_{mix} across AR7W-North, providing motivation to study the use of altimeter-derived diffusivity in the LS.

For a further study, we suggest estimating the kc_e^{-1} North-West of AR7W-North, in the region of high IR EKE. Should the study employ the same methodology as that used here, a better estimate of across-jet distance Y could potentially be obtained. Since Tang et al. (1996) find the velocity structure in the LS to only be completely described by both density and topography, Y could be better defined by considering the joint effect of baroclinicity and relief. This may allow tracer gradients to be resolved better, providing a greater selection of reliable results. A similar mixing-length based analysis may benefit from using ARGO data when the spatial sampling resolution in the LS is sufficient.

9: References

Armi, L., & Stommel, H. (1983). Four views of a portion of the North Atlantic subtropical gyre. *Journal of Physical Oceanography*, *13*(5), 828-857.

Chanut, J., Barnier, B., Large, W., Debreu, L., Penduff, T., Molines, J. M., & Mathiot, P. (2008). Mesoscale eddies in the Labrador Sea and their contribution to convection and restratification. *Journal of Physical Oceanography*, *38*(8), 1617-1643.

Chelton, D. B., Schlax, M. G., Samelson, R. M., & de Szoeke, R. A. (2007). Global observations of large oceanic eddies. *Geophysical Research Letters*, *34*(15).

Cunningham, S. A., & Haine, T. W. (1995). Labrador Sea Water in the eastern North Atlantic. Part II: Mixing dynamics and the advective-diffusive balance. *Journal of Physical Oceanography*, *25*(4), 666-678.

Cuny, J., Rhines, P. B., Niiler, P. P., & Bacon, S. (2002). Labrador Sea boundary currents and the fate of the Irminger Sea Water. *Journal of Physical Oceanography*, *32*(2), 627-647.

Curry, R. G., & McCartney, M. S. (2001). Ocean Gyre Circulation Changes Associated with the North Atlantic Oscillation. *Journal of Physical Oceanography*, *31*(12), 3374-3400.

Dickson, R., Osborn, J., Hurrell, W., Meincke, J., Blindheim, J., Adlandsvik, B., & Co Authors (2000). The Arctic Ocean response to the North Atlantic Oscillation. *Journal of Climate*, *13*(15), 2671-2696.

Dickson, R., Rudels, B., Dye, S., Karcher, M., Meincke, J. & Yashayaev, I. (2007). Current estimates of freshwater flux through Arctic and subarctic seas. *Progress in Oceanography*, *73*(3), 210-230.

Dansgaard, W., Johnsen, S. J., Clausen, H. B., Dahl-Jensen, D., Gundestrup, N. S., Hammer, C. U., & Co-Authors (1993). Evidence for general instability of past climate from a 250-kyr ice-core record. *Nature*, *364*(6434), 218-220.

Ferrari, R., & Nikurashin, M. (2010). Suppression of eddy diffusivity across jets in the Southern Ocean. *Journal of Physical Oceanography*, *40*(7), 1501-1519.

Ferrari, R., & Polzin, K. L. (2005). Finescale structure of the T-S relation in the eastern North Atlantic. *Journal of physical oceanography*, *35*(8), 1437-1454.

Frajka-Williams, E., Rhines, P. B., & Eriksen, C. C. (2014). Horizontal Stratification during Deep Convection in the Labrador Sea. *Journal of Physical Oceanography*, *44*(1), 220-228.

Gelderloos, R., Katsman, C. A., & Drijfhout, S. S. (2011). Assessing the roles of three eddy types in restratifying the Labrador Sea after deep convection. *Journal of Physical Oceanography*, *41*(11), 2102-2119.

Gent, P. R., & Mcwilliams, J. C. (1990). Isopycnal mixing in ocean circulation models. *Journal of Physical Oceanography*, *20*(1), 150-155.

Haak, H., Jungclaus, J., Koenigk, T., Sein, D., & Mikolajewicz, U. (2005). Arctic Ocean freshwater budget variability. *Arctic Subarctic Ocean Fluxes (ASOF) Newsletter*, 3, 6-8.

Hofmann, M., & Rahmstorf, S. (2009). On the stability of the Atlantic Meridional Overturning Circulation. *Proceedings of the National Academy of Sciences*, *106*(49), 20584-20589.

Holloway, G. (1986). Estimation of oceanic eddy transports from satellite altimetry. *Nature,* 323(6085), 243-244.

Hu, A., Meehl, G. A., Han, W., Otto-Bliestner, B., Abe-Ouchi, A., & Rosenbloom, N. (2014). Effects of the Bering Strait closure on AMOC and global climate under different background climates. *Progress in Oceanography*. ISSN 0079-6611.

Huntington, T. G. (2006). Evidence for intensification of the global water cycle: review and synthesis. *Journal of Hydrology*, *319*(1), 83-95.

Jones, H., & Marshall, J. (1997). Restratification after deep convection. *Journal of Physical Oceanography*, *27*(10), 2276-2287.

Katsman, C. A., Spall, M. A., & Pickart, R. S. (2004). Boundary Current Eddies and Their Role in the Restratification of the Labrador Sea. *Journal of physical oceanography*, *34*(9), 1967-1983.

Kawasaki, T., & Hasumi, H. (2014). Effect of freshwater from the WGC on the winter deep convection in the Labrador Sea. *Ocean Modelling*, *75*, 51-64.

Keffer, T., & Holloway, G. (1988). Estimating Southern Ocean eddy flux of heat and salt from satellite altimetry. *Nature,* 332(6165), 624-626.

Khatiwala, S., Schlosser, P., & Visbeck, M. (2002). Rates and Mechanisms of Water Mass Transformation in the Labrador Sea as Inferred from Tracer Observations. *Journal of Physical Oceanography*, *32*(2), 666-686.

Kuhlbrodt, T., Griesel, A., Montoya, M., Levermann, A., Hofmann, M., & Rahmstorf, S. (2007). On the driving processes of the Atlantic Meridional Overturning Circulation. *Reviews of Geophysics*, *45*(2).

Kwok, R., Cunningham, G. F., & Pang, S. S. (2004). Fram Strait sea ice outflow. *Journal of Geophysical Research: Oceans (1978–2012)*, *109*(C1).

Lazier, J., Hendry, R., Clarke, A., Yashayaev, I., & Rhines, P. (2002). Convection and restratification in the Labrador Sea, 1990–2000. *Deep Sea Research Part I: Oceanographic Research Papers*, *49*(10), 1819-1835.

Lindsay, R. W., & Zhang, J. (2005). The thinning of Arctic sea ice, 1988-2003: Have we passed a tipping point? *Journal of Climate*, *18*(22), 4879-4894.

Lilly, J. M., Rhines, P. B., Visbeck, M., Davis, R., Lazier, J. R., Schott, F., & Farmer, D. (1999). Observing deep convection in the Labrador Sea during winter 1994/95. *Journal of Physical Oceanography*, *29*(8), 2065-2098.

Liu, W., Liu, Z., & Brady, E. C. (2014). Why is the AMOC Monostable in Coupled General Circulation Models? *Journal of Climate*, *27*(6), 2427-2443.

Luo, H., Bracco, A., Yashayaev, I., & Di Lorenzo, E. (2012). The interannual variability of potential temperature in the central Labrador Sea. *Journal of Geophysical Research: Oceans (1978–2012)*, *117*(C10).

Ledwell, J. R., Watson, A. J., & Law, C. S. (1993). Evidence for slow mixing across the pycnocline from an open-ocean tracer-release experiment. *Nature*, *364*(6439), 701-703.

Marotzke, J. (2012). Climate science: A grip on ice-age ocean circulation. *Nature*, *485*(7397), 180-181.

McGeehan, T., & Maslowski, W. (2011). Impact of shelf-basin freshwater transport on deep convection in the western Labrador Sea. *Journal of Physical Oceanography*, *41*(11), 2187-2210.

Mizoguchi, K. I., Morey, S. L., Zavala-Hidalgo, J., Suginohara, N., Häkkinen, S., & O'Brien, J. J. (2003). Convective activity in the Labrador Sea: Preconditioning associated with decadal variability in subsurface ocean stratification. *Journal of Geophysical Research: Oceans (1978–2012)*, *108*(C10).

Myers, P. G. (2005). Impact of freshwater from the Canadian Arctic Archipelago on Labrador Sea Water formation. *Geophysical Research Letters*, *32*(6).

Myers, P. G., Donnelly, C., & Ribergaard, M. H. (2009). Structure and variability of the WGC in summer derived from 6 repeat standard sections. *Progress in Oceanography*, *80*(1), 93-112.

Naveira Garabato, A. C., Ferrari, R., & Polzin, K. L. (2011). Eddy stirring in the Southern Ocean. *Journal of Geophysical Research: Oceans (1978–2012)*, *116*(C9).

Rahmstorf, S. (1996). On the freshwater forcing and transport of the Atlantic thermohaline circulation. *Climate Dynamics*, *12*(12), 799-811.

Schmidt, S., & Send, U. (2007). Origin and composition of seasonal Labrador Sea freshwater. *Journal of physical oceanography*, *37*(6), 1445-1454.

Sijp, W. P. (2012). Characterising meridional overturning bistability using a minimal set of state variables. *Climate dynamics*, *39*(9-10), 2127-2142.

Stammer, D. (1998). On eddy characteristics, eddy transports, and mean flow properties. *Journal of Physical Oceanography*, *28*(4), 727-739.

Straneo, F. (2006). Heat and Freshwater Transport through the Central Labrador Sea. Journal of Physical Oceanography, 36(4), 606-628.

Straneo, F., Pickart, R. S., & Lavender, K. (2003). Spreading of Labrador Sea water: An advective-diffusive study based on Lagrangian data. *Deep Sea Research Part I: Oceanographic Research Papers*, *50*(6), 701-719.

Straneo, F., & Saucier, F. (2008). The outflow from Hudson Strait and its contribution to the LC. *Deep Sea Research Part I: Oceanographic Research Papers*, *55*(8), 926-946.

Tang, C. C., Gui, Q., & Peterson, I. K. (1996). Modeling the mean circulation of the Labrador Sea and the adjacent shelves. *Journal of physical oceanography*, *26*(10), 1989-2010.

Tang, C. C., Ross, C. K., Yao, T., Petrie, B., DeTracey, B. M., & Dunlap, E. (2004). The circulation, water masses and sea-ice of Baffin Bay. *Progress in Oceanography*, *63*(4), 183-228.

The Lab Sea Group (1998). The Labrador Sea deep convection experiment. *Bulletin of the American Meteorological Society*, *79*(10), 2033-2058.

Thomsen, S., Eden, C., & Czeschel, L. (2013). Stability analysis of the LC. *Journal of Physical Oceanography*, *44*(2), 445-463.

Våge, K., Pickart, R. S., Moore, G. W. K., & Ribergaard, M. H. (2008). Winter mixed layer development in the central Irminger Sea: The effect of strong, intermittent wind events. *Journal of Physical Oceanography*, *38*(3), 541-565.

Walker, H. M. (1940). Degrees of freedom. *Journal of Educational Psychology*, *31*(4), 253.

Wu, P., Wood, R., & Stott, P. (2005). Human influence on increasing Arctic river discharges. *Geophysical Research Letters*, *32*(2).

Wunsch, C. (1999). Where do ocean eddy heat fluxes matter? *Journal of Geophysical Research: Oceans (1978–2012)*, *104*(C6), 13235-13249.

Yashayaev, I., Bersch, M., & van Aken, H. M. (2007). Spreading of the Labrador Sea Water to the Irminger and Iceland basins. *Geophysical Research Letters*, *34*(10).